

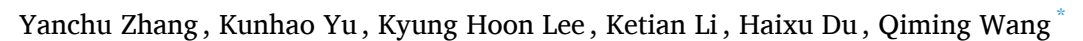
Contents lists available at ScienceDirect

Journal of the Mechanics and Physics of Solids

journal homepage: www.elsevier.com/locate/jmps



Mechanics of stretchy elastomer lattices



Sonny Astani Department of Civil and Environmental Engineering, University of Southern California, Los Angeles, CA 90089, United States

ARTICLE INFO

Keywords: Mechanical metamaterials Architected lattices Hierarchical lattices Network model Affine deformation

ABSTRACT

The recent advances in soft matter and advanced manufacturing have enabled the design and fabrication of elastomer lattices for versatile engineering applications. Compared with conventional engineering structures, elastomer lattices exhibit ultra-high reversible stretchability, while maintaining relatively low density. Mechanistic understanding of the mechanics of elastomer lattices is of great importance for their structural design and optimization. However, the existing studies in this field are limited to empirical models or finite element methods, while the theoretical modeling remains largely unexplored. This work reports a class of theoretical models for the mechanics of elastomer lattices over finite deformation. The potential energy function is constructed as a superposition of the stretching and bending modes, which are associated with the elongation and rotation of lattice beams, respectively. The stress-stretch behavior is determined with the aid of the principle of stationary potential energy. The model is then extended to explain the mechanics of hierarchical elastomer lattices by introducing the principal stretches in each hierarchical order as generalized coordinates. A set of holonomic constraint equations are written to define the kinematic compatibility and uniaxial stress state for hierarchical lattices, which are numerically solved via a nonlinear optimization algorithm. Results from the proposed theoretical models agree well with finite-element simulations and experiments. Case studies are performed for various material constitutive models, volume fractions, lattice architectures, and deformation modes, demonstrating the generality and robustness of the proposed theoretical models.

1. Introduction

Since the negative Poisson's ratio was discovered on foam structures (Kolpakov, 1985; Lakes, 1987), the research on architected materials has attracted much attention for its versatile applications, especially in energy absorption and impact-resistant devices for biomedical and ergonomic purposes (Evans and Alderson, 2000; Sanami et al., 2014). Another unique negative parameter is the thermal expansion coefficient, as opposed to most solid materials that expand under raised temperatures. Analogous to the molecular and atomic mechanism, the negative thermal expansion was achieved by artificially triggering the beam deformation in the lattice, during which the constituent beam elements would rotate and occupy the internal space, macroscopically exhibiting a volumetric contracting behavior (Lakes, 1996; Wang et al., 2016). Later, the field gradually evolves to engineering new-generation architected materials that are programmed into periodic structures that possess unique mechanical, acoustic, optical, thermal, and electromagnetic properties that are not observed in their constituent materials (Chen et al., 2016; Kadic et al., 2019; Tancogne-Dejean et al., 2018). The realization of the remarkable properties of architected materials does not only depend on the design of the lattice topology but also requires advanced manufacturing techniques. Recent studies in the field of advanced manufacturing have witnessed the

E-mail address: qimingw@usc.edu (Q. Wang).

^{*} Corresponding author.

vibrant development of architected materials made of a variety of constituents, including polymers, ceramics, and metals (Surjadi et al., 2019). These lattice structures with extraordinary properties including low density, high specific stiffness, high specific strength, and high energy absorption, have been used in a broad range of engineering applications, such as aerospace panels, impact absorbers, acoustic modulators, thermal exchangers, battery electrodes, and biomedical scaffolds (Fleck et al., 2010; Gibson and Ashby, 1999; Jens et al., 2017; Montemayor et al., 2015; Roper et al., 2015; Schaedler and Carter, 2016; Surjadi et al., 2019; Wadley, 2006; Xu et al., 2015).

This paper focuses on a class of architected materials that are made of stretchy elastomers to form periodic lattices. Different from most existing lattice structures made of stiff polymers, ceramics, and metals (Surjadi et al., 2019), the elastomer lattices feature high stretchability that is beyond the description of linear elasticity, thus providing a unique structure platform for a number of applications, including soft robotics (Weeger et al., 2019), shape-changing structures (Ji et al., 2019; Ye et al., 2020; Yu et al., 2020), noise-canceling structures (Yu et al., 2018), and energy dissipators (Jiang and Wang, 2016). Despite the great application potential, the theoretical understanding of the mechanics of elastomer lattices has been left behind. So far, most of the theoretical models have concentrated on the stretching-dominated lattice structures via kinematic indeterminacy and force balance analysis (Deshpande et al., 2001; Elsayed and Pasini, 2010). However, the flexural rigidity was not considered in their models, and thus their proposed methods could not be applied to bending-dominated lattices. In addition to the force balance analysis, researchers utilized an alternative energy-based method to predict the mechanical properties of lattice structures. For instance, previous works demonstrated a mesoscale site-bond model for regular-shaped lattices (Berger et al., 2017; Jivkov and Yates, 2012; Wang and Mora, 2008; Zhang et al., 2014). In their analytical model, the strain energy for discrete beam elements was calculated and equivalently homogenized as a continuum unit cell. Although such an energy-based method was mathematically concise, the bending-induced energy was not considered; thus, the site-bond model was only applicable to the stretching-dominated lattices. Inspired by the previous studies, the lattice element method (LEM) was proposed to model the continuum by a lattice unit cell (Laubie et al., 2017a; 2017b). Because their model did not include the flexural rigidity in the effective stiffness tensor, the predicted stiffness of lattice could be underestimated. Having been incorporated with an optimization algorithm to minimize the potential energy, this model worked out the stress distribution around a crack tip, which was verified by analytical solutions in fracture mechanics. Despite the merits of those models for lattice structures under small deformation, the theoretical modeling of elastomer lattices undergoing a finite strain has remained largely unexplored. Researchers tried to fit the experimental stress-strain curves to constitutive models such as the Ogden model and Arruda-Boyce model (Jamshidian et al., 2020; Jiang and Wang, 2016; Li et al., 2017). However, this semi-empirical method did not account for the lattice structural features and kinematics. A general theoretical model coupling kinematic analysis and constitutive models is highly

Although lattice structures are typically classified into stretching-dominated and bending-dominated, it is hypothesized that all lattice structures are stretching-dominated if subjected to a large stretch, regardless of their original classifications in the linear elastic range (Jiang and Wang, 2016; Li et al., 2017). This hypothesis was validated by experimental results and numerical simulations with the finite element method (FEM) (Jiang and Wang, 2016). However, a corresponding theoretical model has not been developed yet, and thus the theoretical explanation for this hypothesis remains unclear. Inspired by the affine deformation assumption in polymer networks (Rubinstein and Panyukov, 2002; Wu and Van Der Giessen, 1993), we postulate that elastomer lattices with regular architectures also follow the affine deformation assumption. Consequently, the stretch of the constituent beam ligament is fully determined with three principal stretches applied to the lattice structure. Once the constitutive models for hyperelastic materials are taken into consideration (Arruda and Boyce, 1993; Ogden, 1972; Rivlin, 1948; Treloar, 1943), a strain energy function embodying the strain energy from discrete beam elements is constructed. Therefore, the discrete beam elements are homogenized to a continuum unit cell, and the stress-strain behavior of the lattice can be obtained from the strain energy function with the work conjugate relation. Our proposed model is not only suitable for typical lattice topologies, but also feasible to describe the mechanical behavior of hierarchical lattices. With the introduction of principal stretches in each hierarchical order as generalized coordinates, the generalized forces are formulated via an analytical mechanics framework. The principle of stationary potential energy is realized numerically with an optimization algorithm by minimizing the strain energy function under constraints of compatibility equations and stress boundary conditions. This work provides a theoretical model for elastomer lattice based on polymer networks theory and variational principles of analytical mechanics, in which a multiscale mechanical problem is abstracted and conceptualized in a higher-order dimension space with differential geometry considerations (Lanczos, 2012).

The structure of this work is organized as follows. Section 2 introduces the experimental fabrication and characterization for the mechanical behavior of various elastomer lattices and the material properties of bulk elastomers. Section 3 develops the theoretical model and strain energy functions for stretching and bending mechanisms. The stress-stretch behaviors for elastomer lattices are explained with the work conjugate relation. Based on this methodology, a generic multiscale model to interpret the mechanical behavior of hierarchical lattices is proposed, with the aid of analytical mechanics and variational principles. In Section 4, several case studies are demonstrated for various lattice structures coupling with different constitutive models. The numerical results are verified with finite element simulations and validated by experimental results to ensure the feasibility and accuracy of the proposed model. Conclusive remarks are summarized in Section 5.

2. Experimental

The fabrication of elastomer lattices started from water-soluble hollow scaffolds that were 3D-printed by a projection microstereolithography system. The photoresin was a mixture of acrylic-based photopolymers N,N-Dimethylacrylamide (40% wt), Methacrylic acid (40% wt) and Methacrylic anhydride (7% wt), water-soluble filler Polyvinylpyrrolidone (11% wt), and photoinitiator

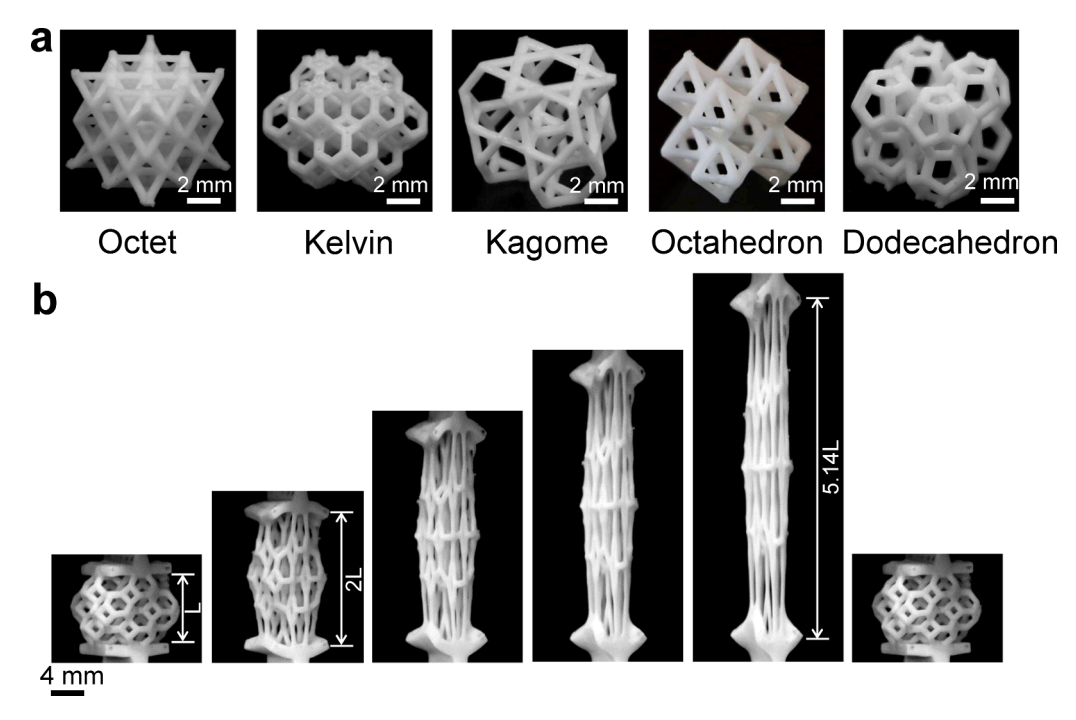


Fig. 1. The fabricated elastomer lattices. (a) The fabricated elastomer lattices in various architectures: Octet-truss, Kelvin, Kagome, Octahedron, and Dodecahedron. (b) Reversible stretching of a Kelvin elastomer lattice.

Phenylbis (2,4,6-trimethylbenzoyl) phosphine oxide (2% wt) (Jiang and Wang, 2016; Li et al., 2017; Liska et al., 2005). Once the hollow scaffolds were 3D-printed, they were air-dried for 2 h. Then, the hollow scaffolds were filled with tin-catalyzed silicone elastomers (mold max NV14 and 10T, Smooth-on, USA) and Urethane elastomers (PMC-724, Smooth-on, USA) with mixtures of the base and the crosslinker 10:1 and 1:1 by weight, respectively. The filled elastomers were cured for 12 h at 25 °C. Thereafter, the composites with scaffolds and cured elastomers were immerged in 1 mol/L NaOH solution for 6 h. The elastomer lattices were ready for use after washing in DI water for 2 min and air-drying for 2 min. In tensile tests, the samples were clamped on the designed stretching bars and stretched by loading rate 0.0167 mm/s with a mechanical tester (model 5942, Instron, USA). The deformation evolution was recorded by a camera (Canon EOS 70D) and the tensile strain was calculated by the real elongating length of the lattice part. The nominal stress was calculated by normalizing the stretching force with the effective cross-section area of the lattice.

The manufacturing method enabled us to fabricate a variety of elastomer lattices with complex 3D architectures (Fig. 1a), such as Octet-truss, Kelvin, Kagome, Octahedron, and Dodecahedron lattices. Taking the Kelvin elastomer lattice as an example, it reversibly sustained 414% uniaxial strain (Fig. 1b). By judicious design, we also fabricated hierarchical elastomer lattices with 3D fractal architectures (Fig. 2). As shown in Fig. 2b, a lattice in self-similar fractal octahedron architectures was fabricated. The employment of 3D fractal architecture can drastically increase structural stretchability (Li et al., 2017). Uniaxial stretching tests showed that the second-order structure (Fig. 2b) exhibited the maximum stretch as high as 7.1 (Fig. 2c), while the maximum stretch for the first-order structure is only 5 (Li et al., 2017).

To understand the mechanics of elastomer lattices, we need to first understand the mechanics of the employed elastomer material. The experimentally measured nominal stress-stretch curve of the elastomer under plane-stress uniaxial tension and compression is shown in Fig. 3, in which the positive stress denotes tension and negative stress denotes compression. The experimentally measured stress-stretch curve can be fitted with various models, including neo-Hookean model, Ogden model, and Arruda-Boyce model (Fig. 3). The corresponding equations for these models are given in Appendix A and the corresponding fitted parameters are shown in Table 1. Note that the neo-Hookean model cannot capture the experimentally measured stress-stretch behavior for stretches higher than 3.5 because the neo-Hookean model does not account for the stiffening effect at high stretches of the elastomer.

3. Theoretical model

3.1. Problem statement

A theoretical model to describe the mechanical behavior of a hierarchical lattice will be introduced with the second-order Octahedral lattice as an example (Fig. 4). The first-order structure is regarded as a minimum repeated unit cell in the fractal lattice. In this way, the second-order lattice can be assembled by replacing each beam ligament in the first-order lattice with another two first-order unit cells, forming a self-similar fractal lattice. In the second-order lattice, some small segments are embedded at the joint corners to reduce the unit cell size and avoid the overlap between unit cells. Downscaling from the first-order lattice, the polymer network defines

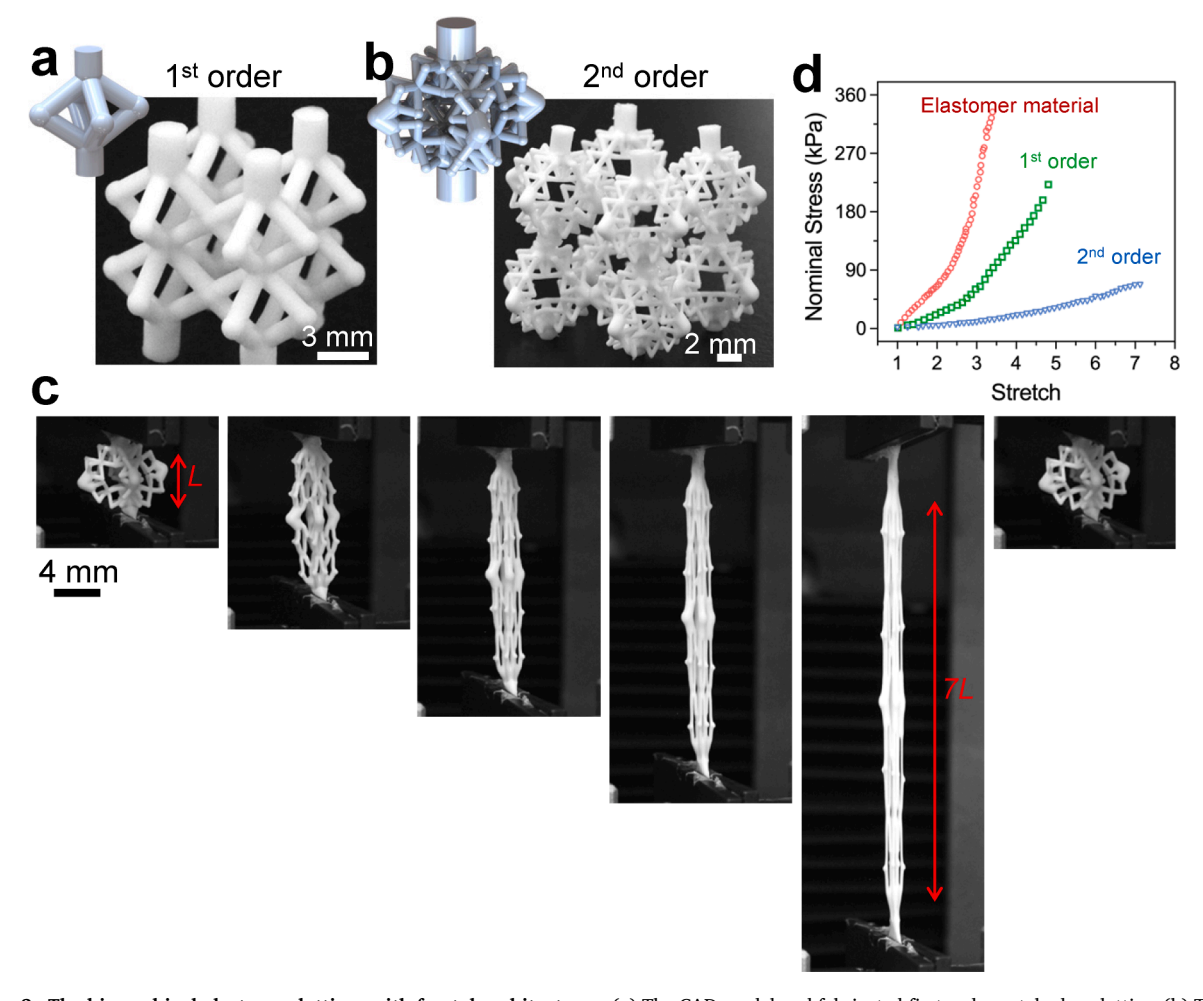


Fig. 2. The hierarchical elastomer lattices with fractal architectures. (a) The CAD model and fabricated first-order octahedron lattice. (b) The CAD model and fabricated second-order hierarchical lattice. (c) Reversible stretching of the hierarchical elastomer lattice. (d) Experimentally measured nominal stress-stretch results for the elastomer material (0th order), 1st order lattice, and 2nd order lattice.

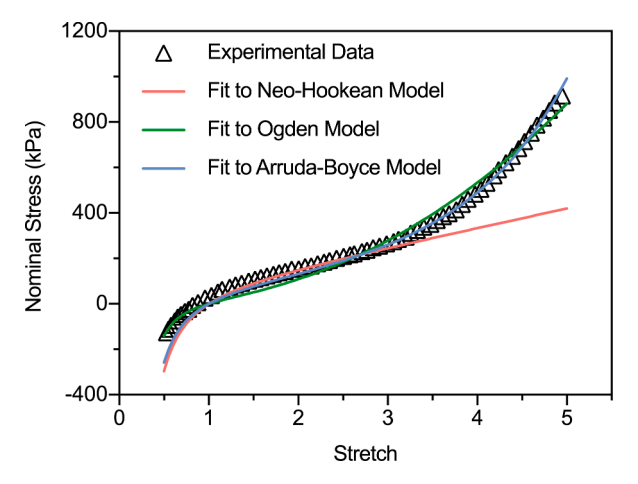


Fig. 3. Experimentally measured stress-stretch behavior of the elastomer material and its fitting with three constitutive models including neo-Hookean model, Ogden model, and Arruda-Boyce model. The negative stress part indicates the compression.

Table 1Fitting parameters for three constitutive models. The symbols are defined in Appendix A.

Models	Parameters
Neo-Hookean	$\mu_0 = 84.60 \text{ kPa}$
Ogden (order 1)	$\mu_1 = 38.03 \; \mathrm{kPa}, \; \alpha_1 = 3.26$
Arruda-Boyce	$\mu_0 = 68.22 \; \mathrm{kPa}, \; \lambda_m = 2.86$

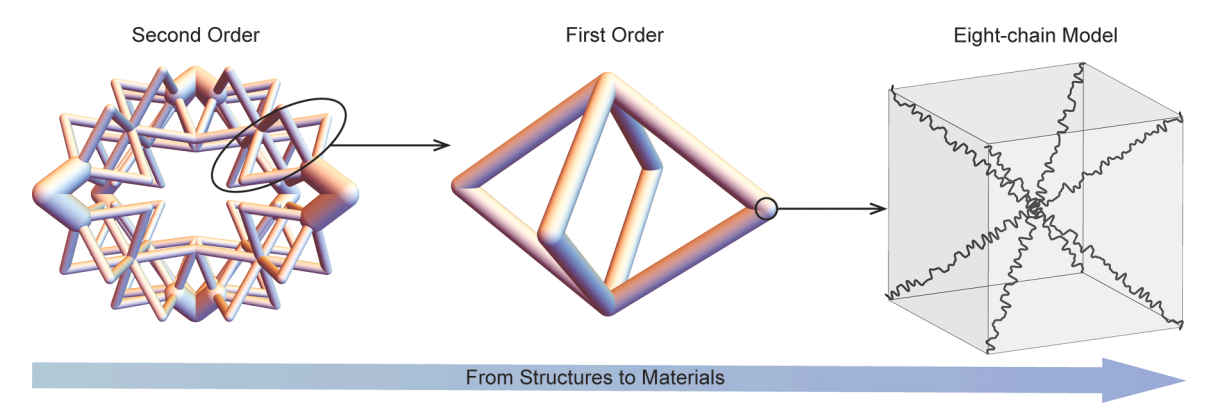


Fig. 4. Breakdown schematic illustration of a hierarchical Octahedral lattice.

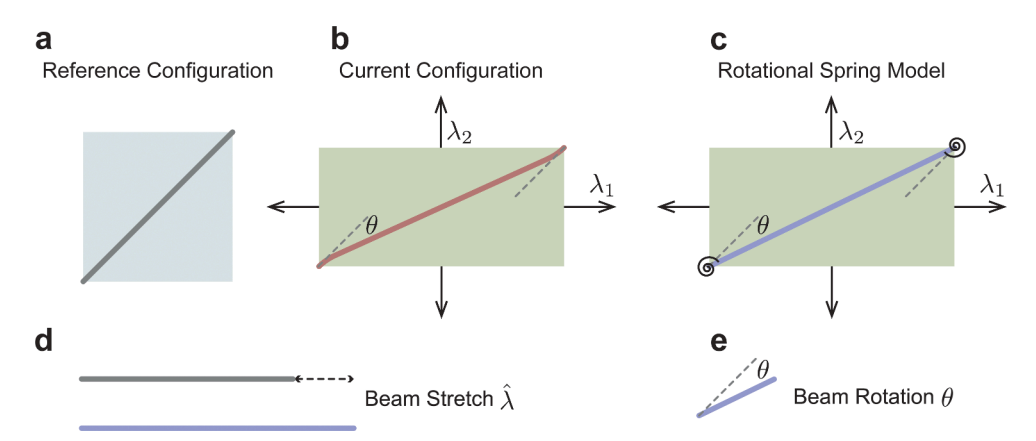


Fig. 5. Schematic illustrations of the kinematics of a beam subjected to principal stretches λ_1 and λ_2 . (a) The reference configuration. (b) The current configuration. (c) A rotational spring model to approximate the bending. (d) Local beam stretch. (e) Local beam rotation.

the constitutive model for elastomers. Having considered both the structural features and material properties, the proposed model can interpret the physics and capture the mechanical behavior of elastomer lattices.

For a lattice subjected to an increasing stretch, the beam ligaments will be gradually aligned to the stretching direction, exhibiting a low initial stiffness. During the beam alignment process, the dominant deformation pattern is primarily governed by bending behavior. Therefore, the introduction of bending-induced strain energy is of vital importance to predict the compliant behavior during the beam alignment process.

Under a set of principal stretches λ_1 , λ_2 , and λ_3 , it is assumed that the unit cell undergoes an affine deformation from its reference configuration, which is schematically demonstrated in **Figs. 5ab**. The beam ligament is stretched along its longitude direction except for a curl observed at both endpoints, attributed to the bending moment and the corresponding flexural stress. The deformed ligament can be approximately considered as a stretching rod with two rotational springs connected at both ends, as illustrated in **Fig. 5c**. Once the applied stretches on the lattice are given, the resulting beam stretch $\hat{\lambda}$ and rotation angle θ , which are illustrated in **Figs. 5de**, are uniquely determined through a kinematic analysis presented in the following subsections.

Considering the approximation in Fig. 5, the strain energy is composed of two parts, namely, stretching and bending, which will be introduced in the following two separate subsections. The theoretical derivations for various lattice structures and constitutive models are similar. Therefore, the subsequent efforts will mainly focus on the Octahedral lattice with the Arruda-Boyce model as the

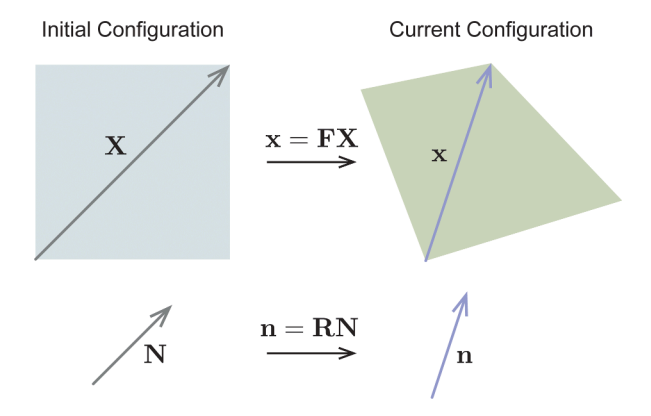


Fig. 6. Schematic illustrations of vectors \mathbf{X} and \mathbf{x} with their directional cosine vectors \mathbf{N} and \mathbf{n} during deformation.

representative example. The derivations for other lattices, including the Octet-truss and Kelvin lattice with the neo-Hookean model, Ogden model, and Arruda-Boyce model, are documented in Appendix B.

3.2. Stretching model for a unit cell lattice

The lattice structure, which consists of discrete beam ligaments, is identically represented by a continuum unit cell with identical effective material and geometric properties. The kinematics of an affine deformation yields the relation of a vector segment featuring a beam ligament between the reference and current configurations such that

$$\mathbf{x} = \mathbf{F}\mathbf{X},\tag{1}$$

where $\mathbf{F} = \mathbf{x} \otimes \nabla$ is the deformation gradient, and the vector segments \mathbf{x} and \mathbf{X} are denoted by their length l and L, together with their directional cosine vectors \mathbf{n} and \mathbf{N} such that

$$\mathbf{x} = l\mathbf{n}, \quad \mathbf{X} = L\mathbf{N}.$$
 (2)

The vectors previously mentioned are schematically illustrated in Fig. 6. From the reference configuration to the current configuration, the vector \mathbf{X} is deformed into \mathbf{x} via Piola transform, with the length elongating from L to L. In contrast, the directional vector remains its length during deformation, which is mathematically written as $\sqrt{\mathbf{N}^2} = \sqrt{\mathbf{n}^2} = 1$. Therefore, the vector \mathbf{N} is deformed into \mathbf{n} via isometric transformation as

$$\mathbf{n} = \mathbf{R}\mathbf{N},\tag{3}$$

where \mathbf{R} is a rotation matrix.

Combining Eqs. (1) and 2 produces the uniaxial beam stretch $\hat{\lambda}$ as

$$\hat{\lambda}^2 = \frac{l^2}{L^2} = \mathbf{N} \cdot \mathbf{F}^{\mathrm{T}} \mathbf{F} \mathbf{N} = \mathbf{N} \cdot \mathbf{C} \mathbf{N},\tag{4}$$

where $C = F^T F$ denotes the right Cauchy-Green deformation tensor.

Given the direction of the beam ligament N and the predefined deformation gradient F, the uniaxial beam stretch can be determined via Eq. (4) as $\hat{\lambda} = \sqrt{N \cdot CN}$. The relation between directional vectors n and N in Eq. (3) could be simplified by combining Eqs. (1) to 4 as

$$\mathbf{n} = \frac{L}{l}\mathbf{F}\mathbf{N} = \frac{\mathbf{F}}{\hat{\lambda}}\mathbf{N},\tag{5}$$

where the rotation matrix is obtained as

$$\mathbf{R} = \frac{\mathbf{F}}{\hat{\lambda}} = \frac{\mathbf{F}}{\sqrt{\mathbf{N} \cdot \mathbf{C} \mathbf{N}}}.$$
 (6)

Note that the set of rotation matrix \mathbf{R} is not an SO(3) (three-dimensional special orthogonal) group, due to the following inequalities.

$$det(\mathbf{R}) = \frac{det(\mathbf{F})}{\sqrt{\mathbf{N} \cdot \mathbf{C} \mathbf{N}}} \neq \pm 1; \tag{7}$$

$$\mathbf{R}^{\mathrm{T}}\mathbf{R} = \frac{\mathbf{F}^{\mathrm{T}}\mathbf{F}}{\mathbf{N} \cdot \mathbf{C}\mathbf{N}} = \frac{\mathbf{C}}{\mathbf{N} \cdot \mathbf{C}\mathbf{N}} \neq \mathbf{I},$$
 (8)

where I is the unit matrix or Kronecker delta.

In the case where the deformation gradient is a diagonal tensor with three principal values, i.e., λ_1 , λ_2 , and λ_3 , the previously obtained Eqs. (4) and 6 are explicitly written as

$$\widehat{\lambda} = \sqrt{N_1^2 \lambda_1^2 + N_2^2 \lambda_2^2 + N_3^2 \lambda_3^2},\tag{9}$$

$$\mathbf{R} = \frac{\lambda_1 \mathbf{g}_1 \otimes \mathbf{G}_1 + \lambda_2 \mathbf{g}_2 \otimes \mathbf{G}_2 + \lambda_3 \mathbf{g}_3 \otimes \mathbf{G}_3}{\sqrt{N_1^2 \lambda_1^2 + N_2^2 \lambda_2^2 + N_3^2 \lambda_3^2}},$$
(10)

where G_i and g_i are base vectors in the reference configuration and current configuration, respectively.

Note that the above analyses Eqs. (1)-(10) are based on the affine deformation assumption of elastomer lattices. To verify the affine deformation assumption, we add Appendix B to compare the theoretical models for the beam deformation with the respective finite element simulation results (Figs. B1-B3). The results shown in Appendix B clearly justify the validity of the affine deformation assumption for the elastomer lattices studied in this paper.

For an incompressible material under uniaxial stretch, the principal stretches $\hat{\lambda}_i$ can be formulated as $\hat{\lambda}_1 = \hat{\lambda}$, $\hat{\lambda}_2 = 1/\sqrt{\hat{\lambda}}$, and $\hat{\lambda}_3 = 1/\sqrt{\hat{\lambda}}$, and thus the incompressible condition $\det \mathbf{F} = \hat{\lambda}_1 \hat{\lambda}_2 \hat{\lambda}_3 = 1$ is automatically satisfied. The strain energy density function \widehat{W} for a single beam ligament is formulated with Arruda-Boyce model as (Arruda and Boyce, 1993)

$$\widehat{W} = \mu_0 \left[\frac{1}{2} (\widehat{I}_1 - 3) + \frac{1}{20\lambda_m^2} (\widehat{I}_1^2 - 9) + \frac{11}{1050\lambda_m^4} (\widehat{I}_1^3 - 27) \right], \tag{11}$$

where μ_0 denotes the shear modulus for bulk materials, $\hat{I}_1 = \hat{\lambda}^2 + 2/\hat{\lambda}$ denotes the first invariant of the right Cauchy-Green tensor for a beam ligament under uniaxial tension, and λ_m denotes the stretchability of the elastomer. Because the incompressible condition is already presumed, it is identical to introducing a Lagrange multiplier in Eq. (11).

By taking advantage of the symmetry of an Octahedral lattice, one can readily write the directional cosine vector as

$$\mathbf{N} = \pm \frac{1}{\sqrt{3}} \mathbf{G}_1 \pm \frac{1}{\sqrt{3}} \mathbf{G}_2 \pm \frac{1}{\sqrt{3}} \mathbf{G}_3, \tag{12}$$

which can be observed in Figs. 2a and 4.

Given the geometry of an Octahedral lattice, the local beam stretch in Eq. (4) is explicitly written as

$$\widehat{\lambda} = \sqrt{\frac{\lambda_1^2 + \lambda_2^2 + \lambda_3^2}{3}} = \sqrt{\frac{I_1}{3}},\tag{13}$$

where $I_1 = \lambda_1^2 + \lambda_2^2 + \lambda_3^2$ is the first invariant of the right Cauchy-Green tensor for the overall lattice structure. It is highlighted that the two invariants \hat{I}_1 and I_1 are defined in the local coordinate in beam ligaments and global coordinate in the lattice structure, respectively. With the aid of Eq. (13), the first invariant of the right Cauchy-Green tensor for the local beam coordinate is obtained as

$$\widehat{I}_{1} = \widehat{\lambda}^{2} + \frac{2}{\widehat{\jmath}} = \left(\frac{I_{1}}{3}\right) + 2\left(\frac{I_{1}}{3}\right)^{-\frac{1}{2}}.$$
(14)

Then, the strain energy function in Eq. (11) could be further simplified for an Octahedral lattice as

$$\widehat{W} = \mu_0 \left(\frac{1}{2} \left[\left(\frac{I_1}{3} \right) + 2 \left(\frac{I_1}{3} \right)^{-\frac{1}{2}} - 3 \right] + \frac{1}{20\lambda_m^2} \left[\left(\frac{I_1}{3} \right)^2 + 4 \left(\frac{I_1}{3} \right)^{\frac{1}{2}} + 4 \left(\frac{I_1}{3} \right)^{-1} - 9 \right] + \frac{11}{1050\lambda_m^4} \left[\left(\frac{I_1}{3} \right)^3 + 6 \left(\frac{I_1}{3} \right)^{\frac{3}{2}} + 8 \left(\frac{I_1}{3} \right)^{-\frac{3}{2}} - 15 \right] \right).$$
(15)

The Octahedral lattice is homogenized as a continuum unit cell of side length a, which comprises 8 beam ligaments of radius r and length $\sqrt{3}a/2$. Therefore, the strain energy density function for the unit cell lattice is formulated by

$$W(\lambda_{1}, \lambda_{2}, \lambda_{3}) = \frac{\sqrt{3}\pi r^{2}}{2a^{2}} \mu_{0} \left(\frac{1}{2} \left[8 \left(\frac{I_{1}}{3} \right) + 16 \left(\frac{I_{1}}{3} \right)^{-\frac{1}{2}} - 24 \right] \right.$$

$$\left. + \frac{1}{20\lambda_{m}^{2}} \left[8 \left(\frac{I_{1}}{3} \right)^{2} + 32 \left(\frac{I_{1}}{3} \right)^{\frac{1}{2}} + 32 \left(\frac{I_{1}}{3} \right)^{-1} - 72 \right] \right.$$

$$\left. + \frac{11}{1050\lambda_{m}^{4}} \left[8 \left(\frac{I_{1}}{3} \right)^{3} + 48 \left(\frac{I_{1}}{3} \right)^{\frac{3}{2}} + 64 \left(\frac{I_{1}}{3} \right)^{-\frac{3}{2}} - 120 \right] \right).$$

$$(16)$$

Note that the constituent material is incompressible, as indicated in the incompressible condition $\det \mathbf{F} = \hat{\lambda}_1 \hat{\lambda}_2 \hat{\lambda}_3 = 1$. However, the lattice structure is compressible, and thus the lattice stretches λ_1 , λ_2 , and λ_3 are not coupled. Therefore, the strain energy in Eq. (16) does not include the Lagrange multiplier.

The nominal stress of the stretching mode can be obtained by taking the derivative with respect to the stretch such that

$$s_{1_stretch} = \frac{\sqrt{3}\pi r^2}{2a^2} \mu_0 \left(\frac{1}{2} \left[\frac{16}{3} \lambda_1 - \frac{16}{3} \lambda_1 \left(\frac{I_1}{3} \right)^{-\frac{3}{2}} \right] \right.$$

$$\left. + \frac{1}{20\lambda_m^2} \left[\frac{32}{3} \lambda_1 \left(\frac{I_1}{3} \right) + \frac{32}{3} \lambda_1 \left(\frac{I_1}{3} \right)^{-\frac{1}{2}} - \frac{64}{3} \lambda_1 \left(\frac{I_1}{3} \right)^{-2} \right] \right.$$

$$\left. + \frac{11}{1050\lambda_m^4} \left[16\lambda_1 \left(\frac{I_1}{3} \right)^2 + 48\lambda_1 \left(\frac{I_1}{3} \right)^{\frac{1}{2}} - 64\lambda_1 \left(\frac{I_1}{3} \right)^{-\frac{5}{2}} \right] \right),$$

$$(17-1)$$

$$s_{2_stretch} = \frac{\sqrt{3}\pi r^2}{2a^2} \mu_0 \left(\frac{1}{2} \left[\frac{16}{3} \lambda_2 - \frac{16}{3} \lambda_2 \left(\frac{I_1}{3} \right)^{-\frac{3}{2}} \right] \right.$$

$$\left. + \frac{1}{20\lambda_m^2} \left[\frac{32}{3} \lambda_2 \left(\frac{I_1}{3} \right) + \frac{32}{3} \lambda_2 \left(\frac{I_1}{3} \right)^{-\frac{1}{2}} - \frac{64}{3} \lambda_2 \left(\frac{I_1}{3} \right)^{-2} \right] \right.$$

$$\left. + \frac{11}{1050\lambda_m^4} \left[16\lambda_2 \left(\frac{I_1}{3} \right)^2 + 48\lambda_2 \left(\frac{I_1}{3} \right)^{\frac{1}{2}} - 64\lambda_2 \left(\frac{I_1}{3} \right)^{-\frac{5}{2}} \right] \right),$$

$$(17-2)$$

$$s_{3_stretch} = \frac{\sqrt{3}\pi r^2}{2a^2} \mu_0 \left(\frac{1}{2} \left[\frac{16}{3} \lambda_3 - \frac{16}{3} \lambda_3 \left(\frac{I_1}{3} \right)^{-\frac{3}{2}} \right] + \frac{1}{20\lambda_m^2} \left[\frac{32}{3} \lambda_3 \left(\frac{I_1}{3} \right) + \frac{32}{3} \lambda_3 \left(\frac{I_1}{3} \right)^{-\frac{1}{2}} - \frac{64}{3} \lambda_3 \left(\frac{I_1}{3} \right)^{-2} \right] + \frac{11}{1050\lambda_m^4} \left[16\lambda_3 \left(\frac{I_1}{3} \right)^2 + 48\lambda_3 \left(\frac{I_1}{3} \right)^{\frac{1}{2}} - 64\lambda_3 \left(\frac{I_1}{3} \right)^{-\frac{5}{2}} \right] \right).$$

$$(17-3)$$

3.3. Bending model for a unit cell lattice

The strain energy stored in the rotational spring (Fig. 5c) results from the relative rotation between the beam ligament and spring. For simplicity, we herein assume that the spring is ideally linear elastic, indicating that the bending moment is proportional to the rotation angle. The rotation angle is obtained by using the following inner product as

$$\cos\theta = \mathbf{n} \cdot \mathbf{N} = \mathbf{N} \cdot \mathbf{R} \mathbf{N} = \frac{\mathbf{N} \cdot \mathbf{F} \mathbf{N}}{\sqrt{\mathbf{N} \cdot \mathbf{C} \mathbf{N}}}.$$
 (18)

For an Octahedral lattice, the directional cosine vector is given as $\mathbf{N} = (\pm 1/\sqrt{3}, \pm 1/\sqrt{3})$, as indicated in Eq. (12). Therefore, the numerator in Eq. (18) could be simplified as $\mathbf{N} \cdot \mathbf{F} \mathbf{N} = \lambda_1 + \lambda_2 + \lambda_3/3 = F_{kk}/3$, and the strain energy V stored in a rotational spring of stiffness β is formulated as follows

$$V = \frac{1}{2a^3}\beta\theta^2 = \frac{1}{2a^3}\beta\arccos^2\left(\frac{F_{kk}}{\sqrt{3I_1}}\right),\tag{19}$$

where F_{kk} is the trace or the first invariant of the deformation gradient F.

By correlating to the beam theory with linear elasticity, the spring stiffness is equivalent to the flexural rigidity of an antisymmetric bending beam such that

$$\beta = \frac{12EI}{L},\tag{20}$$

where EI/L is the flexural rigidity. To address the non-linear behavior of the spring stiffness, a more accurate FEM-assisted calibration will be performed for the hierarchical lattice in the next section.

With Eq. (19), the additional stress resulting from the bending is obtained by taking the derivative with respect to the stretch such that

$$s_{1_bend} = \frac{\partial V}{\partial \lambda_1} = -\frac{\beta}{a^3} \arccos\left(\frac{F_{kk}}{\sqrt{3I_1}}\right) \frac{I_1 - \lambda_1 F_{ii}}{I_1 \sqrt{3I_1 - F_{ij}^2}};$$
(21-1)

$$s_{2_bend} = \frac{\partial V}{\partial \lambda_2} = -\frac{\beta}{a^3} \arccos\left(\frac{F_{kk}}{\sqrt{3I_1}}\right) \frac{I_1 - \lambda_2 F_{ii}}{I_1 \sqrt{3I_1 - F_{ij}^2}};$$
(21-2)

$$s_{3_bend} = \frac{\partial V}{\partial \lambda_3} = -\frac{\beta}{a^3} \arccos\left(\frac{F_{kk}}{\sqrt{3I_1}}\right) \frac{I_1 - \lambda_3 F_{ii}}{I_1 \sqrt{3I_1 - F_{ii}^2}}.$$
(21-3)

Integrating Eqs. 17 and 21, we obtain the effective nominal stress in three principal directions written as

$$s_1 = s_{1_stretch} + s_{1_bend}; \tag{22-1}$$

$$s_2 = s_{2_stretch} + s_{2_bend};$$
 (22–2)

$$s_3 = s_{3_stretch} + s_{3_bend}. \tag{22-3}$$

To theoretically predict the uniaxial behavior of the Octahedral lattice, the traction-free conditions that $s_2 = s_3 = 0$ could be exploited to determine the lateral stretches λ_2 and λ_3 as a function of the applied stretch λ_1 . Eventually, the stress-stretch behavior of a unit cell lattice can be established and elucidated with a concise model that accounts for both structural and material properties.

3.4. Rigid zone model for high-volume-fraction lattices

The models introduced above have established the kinematics and constitutive models for lattice structures. However, as the volume fraction increases, the overlap between beam ligaments cannot be ignored, and thus the effective length of the beam is significantly smaller than its center-to-center length. The joint overlap is usually considered stiffer than the slender beam. Therefore, the joint overlap is approximately modeled as a rigid zone, which is widely used in structural design and analysis in civil engineering (Seo and Jang, 1996).

To quantify the effect of the rigid zone, we assume that a beam is composed of a rigid zone of length δ and a deformable zone of length $L-\delta$ in the initial configuration. After deformation, the deformable zone is stretched to a length of $l-\delta$, while the length of the rigid zone remains the same. Consequently, the deformable zones \mathbf{X}^d and \mathbf{x}^d , which are observed in the initial and current configurations, are written as

$$\mathbf{X}^{d} = (L - \delta)\mathbf{N}, \quad \mathbf{x}^{d} = (l - \delta)\mathbf{n}. \tag{23}$$

With the aid of Eqs. (4) and 5, the deformable zone in the current configuration is simplified as

$$\mathbf{x}^d = \mathbf{x} - \delta \mathbf{n} = L\mathbf{F}\mathbf{N} - \delta \frac{\mathbf{F}\mathbf{N}}{\sqrt{\mathbf{N} \cdot \mathbf{C}\mathbf{N}}},\tag{24}$$

whose length is obtained as

$$\sqrt{\mathbf{x}^d \cdot \mathbf{x}^d} = \sqrt{L^2 \mathbf{N} \cdot \mathbf{C} \mathbf{N} - 2\delta L \sqrt{\mathbf{N} \cdot \mathbf{C} \mathbf{N}} + \delta^2} = \left(L \sqrt{\mathbf{N} \cdot \mathbf{C} \mathbf{N}} - \delta\right). \tag{25}$$

Therefore, the stretch of the deformable zone is calculated as

$$\widehat{\lambda}^{d} = \frac{\sqrt{\mathbf{x}^{d} \cdot \mathbf{x}^{d}}}{\sqrt{\mathbf{X}^{d} \cdot \mathbf{X}^{d}}} = \frac{L\sqrt{\mathbf{N} \cdot \mathbf{C}\mathbf{N}} - \delta}{L - \delta}.$$
(26)

Note that Eq. (4) is a particular case for Eq. (26) when $\delta = 0$. If the rigid zone is considered as $\delta > 0$, then it is apparent that $\widehat{\lambda}^d > \widehat{\lambda}$. This inequality is interpreted as the fact that the deformable zone must be elongated more to compensate for the rigid zone.

3.5. Modeling hierarchical lattice

The extreme flexibility can be designed and achieved with the fractal architecture of the hierarchical structure, in which each order experiences a stretch delay that contributes to macroscopic compliance (Li et al., 2017). To theoretically model the mechanical properties of a hierarchical lattice, this section gives a general formulation to describe the behavior of an n^{th} order Octahedral lattice with the help of analytical mechanics and variational principles.

3.5.1. Mathematical descriptions

The kinematics of a hierarchical Octahedral lattice will be discussed in this subsection. Let the lattice consist of n orders, with the 0^{th} order being the beam ligament made of bulk material and the n^{th} order being the macroscopic lattice structure (example in Fig. 2). The recurrence relation of the stretch between the current i^{th} hierarchical order and the subsequent upscaling $(i+1)^{th}$ order is generalized from Eq. (13) when N_1 , N_2 , $N_3 = \pm 1/\sqrt{3}$, which is written as

$${}^{(i)}\lambda_1^2 = \frac{1}{3}{}^{(i+1)}\lambda_1^2 + \frac{1}{3}{}^{(i+1)}\lambda_2^2 + \frac{1}{3}{}^{(i+1)}\lambda_3^2, \tag{27}$$

where the left superscript (\cdot) denotes the number of hierarchical orders and does not count into the tensorial index notation. By multiplying a factor $1/3^i$ in Eq. (27) and operating a summation from i=1 to n yields the kinematic relation as follows

$${}^{(0)}\lambda_1^2 = \frac{1}{3^n}{}^{(n)}\lambda_1^2 + \sum_{i=1}^n \frac{1}{3^i}{}^{(i)}\lambda_2^2 + \sum_{i=1}^n \frac{1}{3^i}{}^{(i)}\lambda_3^2. \tag{28}$$

Since the kinematic relation in Eq. (28) is expressed in a series form, the convergence criterion will be discussed for a fractal-like lattice with an infinite number of hierarchical orders, namely, the mechanical behavior when $n \to \infty$.

During a uniaxial tension, it is reasonably assumed that each beam ligament is stretched and the substructure contracts in the lateral directions due to the positive Poisson's effect such that

$${}^{(i)}\lambda_1^2 > 1, {}^{(i)}\lambda_2^2 < 1, {}^{(i)}\lambda_2^2 < 1.$$
 (29)

According to Weierstrass M-test (Rudin, 1964), a series converges uniformly if there exists a set of bounded values M_i such that

$$M_i = \frac{1}{3^i} \ge \max\left\{\frac{1}{3^i}{}^{(i)}\lambda_2^2, \ \frac{1}{3^i}{}^{(i)}\lambda_3^2\right\},\tag{30}$$

and the infinite series of the upper bound value M_i also converges such that

$$\sum_{i=1}^{\infty} M_i = \sum_{i=1}^{\infty} \frac{1}{3^i} = \frac{1}{2}.$$
 (31)

Therefore, the upper bound for the beam stretch is determined as follows

$${}^{(0)}\lambda_1^2 \le \lim_{n \to \infty} \frac{1}{3^n} {}^{(n)}\lambda_1^2 + 2\sum_{i=1}^n \frac{1}{3^i} = 1.$$
 (32)

It has been proved and demonstrated in Eqs. (29) and 32 that, for a theoretically infinite number of hierarchical-order structures, the beam stretch must be somewhere between its lower and upper bounds such that

$$1 \le \lim_{n \to \infty} {}^{(0)}\lambda_1^2 \le 1,\tag{33}$$

which simply indicates that the beam stretch will converge to $^{(0)}\lambda_1=1$.

Without the loss of generality, the above proof does not restrict to a specific material constitutive model. For any constitutive model, the strain energy density W is positive definite and is a quadratic homogeneous function. Therefore, the strain energy density W must be zero with the beam stretch $^{(0)}\lambda_1$ converging to 1, which is readily represented by Heine theorem as

$$\lim_{n \to \infty} W(^{(0)}\lambda_1) = \lim_{(0)_{\lambda_1 \to 1}} W(^{(0)}\lambda_1) = 0. \tag{34}$$

The physical meaning to decipher the kinematics is that the beam ligament will keep unstretched even if there is a finite external stretch applied upon the lattice structure. Therefore, a hierarchical lattice structure consisting of an infinite number of orders has no initial stiffness, which is rigorously proved via Weierstrass M-test and the Squeeze theorem (Ablowitz et al., 2003; Pugh and Pugh, 2002). Finally, the strain energy is proved to be zero with the aid of the Heine theorem.

3.5.2. Principle of stationary potential energy

In search of a general description for a hierarchical order lattice, we herein introduce a group of generalized coordinates q_j written as

$$(q_1, q_2, q_3, \dots, q_{3n-1}, q_{3n-2}, q_{3n}) = ({}^{(1)}\lambda_1, {}^{(1)}\lambda_2, {}^{(1)}\lambda_3, \dots, {}^{(n)}\lambda_1, {}^{(n)}\lambda_2, {}^{(n)}\lambda_3), \tag{35}$$

where ${}^{(i)}\lambda_1$, ${}^{(i)}\lambda_2$, and ${}^{(i)}\lambda_3$ correspond to the three principal lattice stretches in the i^{th} order.

As indicated in Eq. (6), the motion of a beam ligament could be considered as a uniaxial stretch $\widehat{\lambda}$ followed by a rigid body rotation, with the deformation gradient decomposed as $\mathbf{F} = \widehat{\lambda} \mathbf{R}$. Therefore, the location vector and rotation vector for a deformable dynamical system are formulated on the current configuration as

$$\mathbf{r} = \mathbf{r}(q_i), \quad \boldsymbol{\theta} = \boldsymbol{\theta}(q_i).$$
 (36)

The generalized force is calculated as

$$Q_{j} = \sum_{i} \mathbf{F}^{i} \cdot \frac{\partial \mathbf{r}^{i}}{\partial q_{j}} = \sum_{i} \mathbf{F}^{i} \cdot \frac{\partial \mathbf{r}^{c}}{\partial q_{j}} + \sum_{i} \mathbf{F}^{i} \cdot \frac{\partial \mathbf{r}^{i/c}}{\partial q_{j}}$$

$$= \mathbf{T} \cdot \frac{\partial \mathbf{r}^{c}}{\partial q_{j}} + \sum_{i} \mathbf{F}^{i} \cdot \frac{\partial \dot{\mathbf{r}}^{i/c}}{\partial \dot{q}_{j}} = \mathbf{T} \cdot \frac{\partial \mathbf{r}^{i}}{\partial q_{j}} + \sum_{i} \mathbf{F}^{i} \cdot \frac{\partial (\boldsymbol{\omega} \times \mathbf{r}^{i/c})}{\partial \dot{q}_{j}}$$

$$= \mathbf{T} \cdot \frac{\partial \mathbf{r}^{c}}{\partial q_{j}} + \sum_{i} \mathbf{r}^{i/c} \times \mathbf{F}^{i} \cdot \frac{\partial \boldsymbol{\omega}}{\partial \dot{q}_{j}}$$

$$= \mathbf{T} \cdot \frac{\partial \mathbf{r}^{c}}{\partial q_{i}} + \boldsymbol{\tau} \cdot \frac{\partial \boldsymbol{\omega}}{\partial \dot{q}_{i}},$$

$$(37)$$

where $\mathbf{r}^i = \mathbf{r}^c + \mathbf{r}^{i/c}$ and $\dot{\mathbf{r}}^{i/c} = \boldsymbol{\omega} \times \mathbf{r}^{i/c}$ define the position and velocity of a point i on a continua body rotating about point c, $\boldsymbol{\omega} = \dot{\boldsymbol{\theta}}$ is the angular velocity of the beam ligament, $\mathbf{T} = \sum_i \mathbf{F}^i$ is the applied resultant force, and $\boldsymbol{\tau} = \sum_i \mathbf{r}^{i/c} \times \mathbf{F}^i$ is the applied resultant moment about point c.

The generalized force of a dynamic system in Eq. (37) implies that both the net force and moment contribute to the virtual work if an admissible virtual displacement is imposed. The resultant force T can be obtained via Castigliano's theorem (Timoshenko, 1983), with the aid of strain energy function defined in Eq. (16), and its contribution to the generalized force is

$$Q_j^T = \frac{\partial W}{\partial \mathbf{r}^c} \cdot \frac{\partial \mathbf{r}^c}{\partial q_i} = \frac{\partial W}{\partial q_i}$$
(38)

With regard to the resultant moment τ , its contribution in the generalized force is formulated as

$$Q_{j}^{r} = \frac{\partial V}{\partial \theta} \cdot \frac{\partial \dot{\theta}}{\partial \dot{q}_{i}} = \frac{\partial V}{\partial \theta} \cdot \frac{\partial \theta}{\partial q_{i}} = \frac{\partial V}{\partial q_{i}}.$$
(39)

On account of a uniaxial stress s_1 applied on the n^{th} order lattice structure, the virtual work done by the external load U is

$$\delta U = s_1 \delta^{(n)} \lambda_1. \tag{40}$$

For the entire n^{th} order hierarchical lattice, the principle of stationary potential energy yields

$$\delta({}^{(n)}W + {}^{(n)}V - U) = 0, \tag{41}$$

where the i^{th} order strain energy functions ${}^{(i)}W$ and ${}^{(i)}V$ are generalized from Eqs. 16 and 19 as

$${}^{(i)}W = A_i \frac{\sqrt{3}\pi r^2}{2a_i^2} \mu_0 \left[\frac{1}{2} (\widehat{I}_1 - 3) + \frac{1}{20\lambda_m^2} (\widehat{I}_1^2 - 9) + \frac{11}{1050\lambda_m^4} (\widehat{I}_1^3 - 27) \right], \tag{42}$$

$${}^{(i)}V = \sum_{p=1}^{i} A_{i-p+1} \frac{1}{2a_p^3} \beta_p \arccos^2 \left(\frac{{}^{(p)}F_{kk}}{\sqrt{3^{(p)}I_1}} \right), \tag{43}$$

where a_i is the side length of the i^{th} unit cell, β_i is the spring stiffness corresponding to the i^{th} unit cell, and A_i is the number of beam ligaments in the i^{th} order unit cell lattice. It is noticed that the stretching energy $^{(i)}W$ is associated with the total number of beam ligaments A_i , whereas the bending energy $^{(i)}V$ is associated with the total number of joints A_{i-p+1} between the $(p+1)^{th}$ order structure and the p^{th} order subsidiary structure. Therefore, a summation over the order p appears in Eq. 43.

The principle of stationary potential energy, which states that the minimum potential energy could be achieved with the desired solutions, provides a variational approach to this problem (Lanczos, 2012). However, the calculation in higher hierarchical order is cumbersome, and thus a general algorithm will be implemented to seek the extremum value of the strain energy with some constraint equations. The potential energy for the entire lattice at the macroscopic order *n* is chosen as the optimal function such that

$$\min^{(n)} \Pi = \min^{\lceil (n)} W + {}^{(n)}V - U \rceil, \tag{44}$$

which is subjected to (n-1) kinematic constraint equations in Eq. 27.

Apart from the kinematic constraints, another 2n constraint equations are needed to satisfy the uniaxial stress state such that

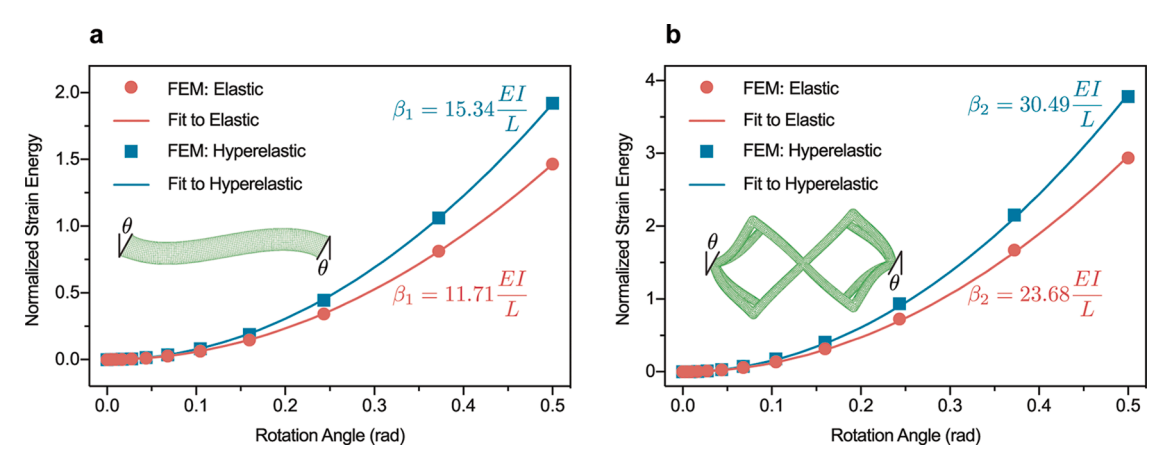


Fig. 7. The total strain energy as a function of rotation angle: (a) in a beam ligament, and (b) in the 1st order lattice.

$$\begin{split} & {}^{(i)}s_2 = \frac{\partial^{(i)}\Pi}{\partial^{(i)}\lambda_2} = \frac{\partial^{(i)}W}{\partial \hat{I}_1} \frac{\partial \hat{I}_1}{\partial^{(i)}\lambda_2} + \frac{\partial^{(i)}V}{\partial^{(i)}F_{kk}} \frac{\partial^{(i)}F_{kk}}{\partial^{(i)}\lambda_2} + \frac{\partial^{(i)}V}{\partial^{(i)}I_1} \frac{\partial^{(i)}I_1}{\partial^{(i)}\lambda_2} \\ & = A_i \frac{\sqrt{3}\pi r^2}{2a_i^2} \mu_0 \left(\frac{1}{2} + \frac{\hat{I}_1}{10\lambda_m^2} + \frac{11\hat{I}_1^2}{350\lambda_m^4} \right) \frac{2^{(i)}\lambda_2}{3^i} \left(1 - \frac{1}{\hat{\lambda}^3} \right) \\ & - \frac{16\beta_i}{a_i^3} \arccos\left(\frac{(i)F_{kk}}{\sqrt{3^{(i)}I_1}} \right) \frac{(i)I_1 - (i)\lambda_2(i)F_{ii}}{(i)I_1\sqrt{3^{(i)}I_1 - (i)}F_{jj}^2} \end{split}$$

$$(45-1)$$

$$\begin{split} & (i)s_{3} = \frac{\partial^{(i)}\Pi}{\partial^{(i)}\lambda_{3}} = \frac{\partial^{(i)}W}{\partial\hat{I}_{1}} \frac{\partial\hat{I}_{1}}{\partial^{(i)}\lambda_{3}} + \frac{\partial^{(i)}V}{\partial^{(i)}F_{kk}} \frac{\partial^{(i)}F_{kk}}{\partial^{(i)}A_{3}} + \frac{\partial^{(i)}V}{\partial^{(i)}I_{1}} \frac{\partial^{(i)}I_{1}}{\partial^{(i)}\lambda_{3}} \\ & = A_{i} \frac{\sqrt{3}\pi r^{2}}{2a_{i}^{2}} \mu_{0} \left(\frac{1}{2} + \frac{\hat{I}_{1}}{10\lambda_{m}^{2}} + \frac{11\hat{I}_{1}^{2}}{350\lambda_{m}^{4}} \right) \frac{2^{(i)}\lambda_{3}}{3^{i}} \left(1 - \frac{1}{\hat{\lambda}^{3}} \right) \\ & - \frac{16\beta_{i}}{a_{i}^{3}} \arccos\left(\frac{(i)F_{kk}}{\sqrt{3^{(i)}I_{1}}} \right) \frac{(i)I_{1} - (i)\lambda_{3}^{(i)}F_{ii}}{(i)I_{1}\sqrt{3^{(i)}I_{1} - (i)}F_{jj}^{2}} \end{split}$$

$$(45-2)$$

With the optimal function and its constraint equations well-defined, a gradient-based optimization algorithm is utilized and performed in MATLAB via the *fmincon* command.

3.5.3. Calibration of the spring stiffness

The spring stiffness is calculated analytically in Eq. (20) for the linear elastic case. In order to extend to hyperelastic material over large deformation, the spring stiffness is herein calibrated with the aid of FEM simulation.

The hierarchical rotational spring β_i describes the bending effects between the i^{th} order lattice and the subsidiary $(i-1)^{th}$ order lattice. Namely, there are n spring constants that need to be determined. Firstly, a beam ligament and a 1^{st} order lattice ligament are modeled in ABAQUS with linear elastic and hyperelastic material properties. In each model, an imposed rotation angle is applied at two opposite ends as displacement boundary conditions. Then the strain energy curves are fitted to the proposed quadratic function in Eq. (19), so that the stiffness constant is numerically obtained. The material properties defined in the simulations are given in Table 1.

The strain energy is extracted from ABAQUS simulations and is then normalized to a dimensionless value by dividing the flexural rigidity EI/L. For a circular beam section with incompressible condition (Poisson's ratio $\nu=0.5$), the Young's modulus and moment of inertia are calculated as

$$E = 2(1+\nu)\mu = 3\mu; \tag{46-1}$$

$$I = \frac{\pi r^4}{4}.\tag{46-2}$$

For the 0th order beam, the fitted curves for elastic material properties and hyperelastic material properties (Arruda-Boyce model) are illustrated in Fig. 7a. It is observed that $\beta_1 = 11.71EI/L$ for the linear elastic case, which is quite close to the analytical prediction that $\beta_1 = 12EI/L$ in Eq. (20). For the hyperelastic case, the stiffness is fitted as $\beta_1 = 15.34EI/L$, which is higher than the linear elastic

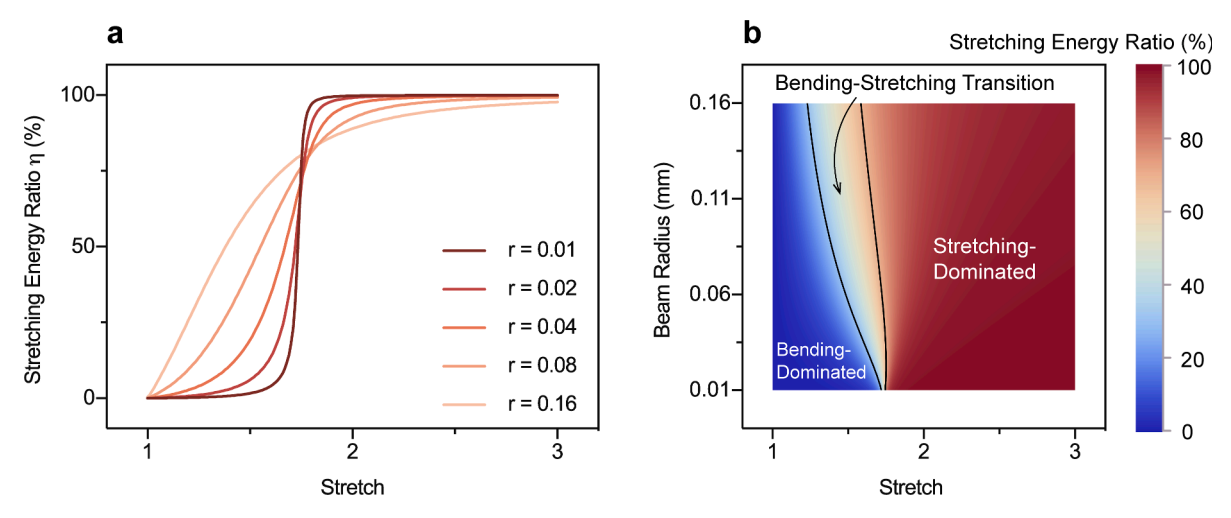


Fig. 8. Visualization of the stretching energy ratio η of Octahedral elastomer lattice. (a) The stretching energy ratio as a function of the applied stretch $\eta(\lambda_1)$ for various beam radii. (b) The stretching energy ratio as a function of applied stretch and beam radius $\eta(\lambda_1, r)$.

prediction. By taking advantage of the FEM-assisted calibration, the linear elastic theory could be readily extended to describe the hyperelastic material properties.

For the 1st order lattice, it is observed that the stiffness β_2 is almost as twice much as the stiffness β_1 , as indicated in Fig. 7b. This relation can be analytically derived for linear elastic case, with the help of structural analysis. Regarding the hyperelastic case, although no analytical solution exists, the doubled stiffness relation is also satisfied. By taking advantage of this observation, we generalize the phenomenological recurrence relation for hierarchical springs as

$$\beta_1 = \frac{15.34EI}{I}, \quad \beta_{i+1} = 2\beta_i. \tag{47}$$

So far, the methodology has been established, and all parameters have been clarified. The numerical verification and experimental validation of our proposed model will be presented in the next section.

4. Results and discussions

The proposed model is validated by comparing the theoretically calculated results with FEM simulations and experimental results. Without the loss of generality, the effects of constitutive models, volume fractions, and lattice architectures are discussed, which prove the feasibility, accuracy, and robustness of our theoretical model.

In the following FEM simulations, all computer-aided design (CAD) models are produced in Solidworks for pre-processing. Afterward, the CAD models are imported into ABAQUS for elastostatic analysis. With the aid of lattice architecture symmetry, the displacements along the normal direction of symmetry planes are prescribed, which are considered as homogeneous Dirichlet boundary conditions. The external load is applied in the form of an imposed displacement along the stretching direction, which is considered as a non-homogeneous Dirichlet boundary condition. Quadratic tetrahedral elements with hybrid formulations (C3D10H) are used for each model. The accuracy and convergence of the FEM results are guaranteed via the comparison with refined meshes. In post-processing, the effective nominal stress of a unit cell is obtained by averaging the reaction force on the plane where the imposed displacement is applied.

4.1. Characterization of the bending and stretching behavior

Previous research work stated that a bending-dominated lattice could exhibit stretching-dominated behavior under large tensile deformation (Jiang and Wang, 2016; Li et al., 2017). This statement was based on phenomenological observation but has not been explored rigorously. With the help of stretching and bending models introduced in Section 3, the total energy is decomposed into stretching-induced energy and bending-induced energy. A parameter η is defined as the ratio between stretching energy and total energy, which is written as

$$\eta(\lambda_1, \lambda_2, \lambda_3) = \frac{W(\lambda_1, \lambda_2, \lambda_3)}{W(\lambda_1, \lambda_2, \lambda_3) + V(\lambda_1, \lambda_2, \lambda_3)}.$$
(48)

Given an Octahedral lattice, the stretching energy ratio η can be calculated as a function of the applied stretch λ_1 . The theoretically predicted stretching energy ratio η is illustrated in Fig. 8. Fig. 8a shows that the function of η appears in the form of a sigmoid function. Initially, η is close to 0%, which indicates that the lattice is bending-dominated. As the stretch increases, the ratio η increases sharply at a certain point and then gradually converges to 100%, indicating that the lattice has switched to stretching-dominated. It is also noted

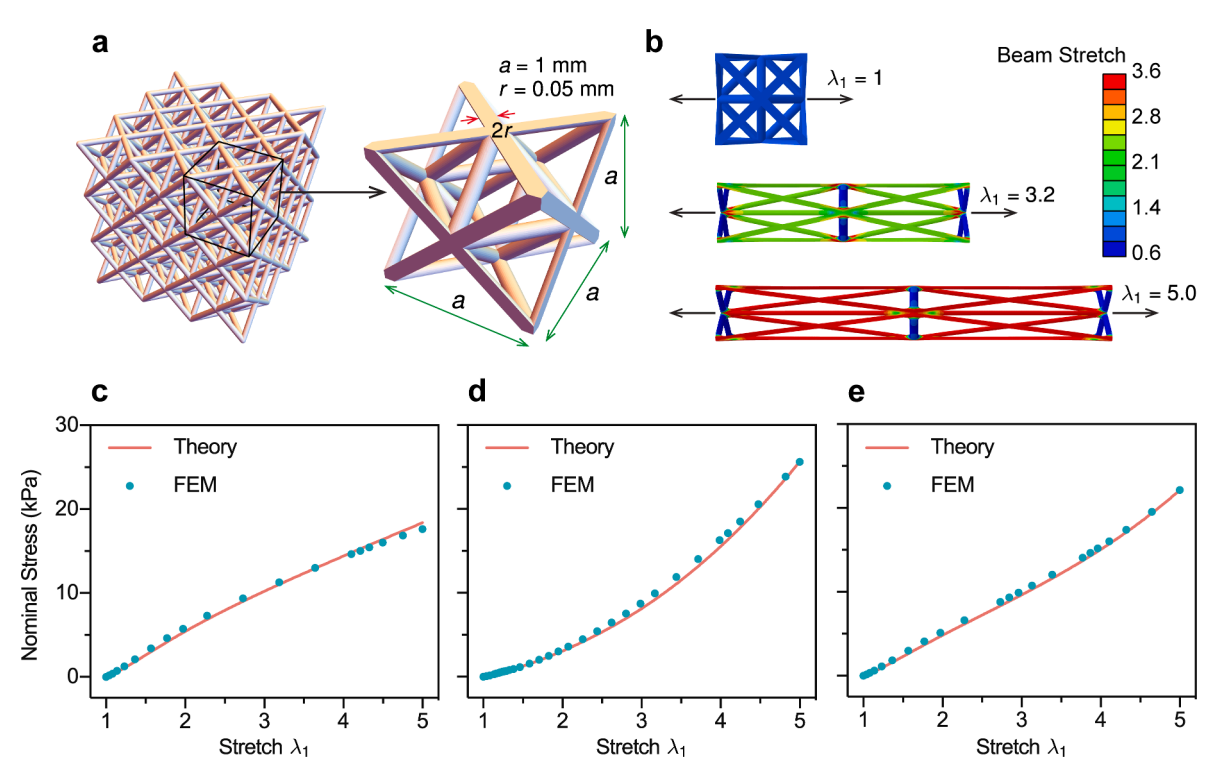


Fig. 9. Case studies for Octet-truss lattices using various constitutive models. (a) CAD models of a 3 by 3 by 3 Octet-truss lattice and the corresponding RVE. (b) Contour plot of beam stretch with the sequential stretching process simulated with ABAQUS (with neo-Hookean model). (c-e) Comparisons between theoretically calculated and FEM-simulated stress-stretch curves with (c) neo-Hookean model, (d) Ogden model, and (e) Arruda-Boyce model.

in Fig. 8b that the lattice with a larger beam radius is more likely to switch to stretching-dominated under small deformation, and it will have a wider bending-stretching transition.

4.2. Effects of constitutive models for octet-truss lattices

The effects of constitutive models on the Octet-truss lattices are discussed in this part. The CAD model of a 3 by 3 by 3 Octet-truss lattice is illustrated in Fig. 9a. A representative volume element (RVE) is partitioned from the periodic lattice. The RVE with side length 1 mm and beam radius 0.05 mm is modeled in ABAQUS. In the post-processing, the sequential stretching process is demonstrated from the reference configuration to the current configuration in Fig. 9b. The contour plot in Fig. 9b indicates the principal stretch in the beam ligament. The stress-stretch behavior of the RVE can be addressed with different constitutive models. For each material model, the theoretical results are compared with the FEM results, which are illustrated in Fig. 9c to e. It is observed in Figs. 9c-e that the proposed model gives an accurate prediction that works well for each constitutive model, which verifies the accuracy and versatility of the proposed model.

4.3. Effects of volume fractions

The scaling law for cellular lattice structures states that the effective modulus is related to the volume fraction by following a power law with the index depending on the lattice architectures (Gibson and Ashby, 1999). A bending-dominated lattice can be switched to stretching-dominated when subjected to large deformation (Jiang and Wang, 2016; Li et al., 2017). There exists a transition that gradually alters the lattice shape to resist stretching. For low volume fraction scenarios, the bending-induced stress is negligible due to the dramatically decreasing flexural rigidity of the beam ligament. As the volume fraction increases, the contribution of bending-induced stress is comparable with the stretching-induced stress. In order to explain the bending-stretching transition, three Octahedral lattices are studied with the same unit cell size and material properties but different beam radii, shown in Figs. 10ab. The comparisons of stress-stretch curves between theoretical and FEM results are illustrated in Figs. 10c-e. In three cases (r = 0.02 - 0.08 mm, Figs. 10c-e), the initial stiffness is relatively small at the initial stretch stage (stretch $s_1 = 1 - 1.7$) while the stiffness drastically increases after stretch $s_1 = 1.7$. The initial small stiffness is because that the extension at the initial stretch stage is due to the beam alignment with a bending mode; once the beam alignment process completes, the beam begins to under a stretching mode with a drastically changed stiffness.

For the high volume fraction case (r = 0.08 mm, Fig. 10e), the initial beam alignment process can induce a relatively large bending

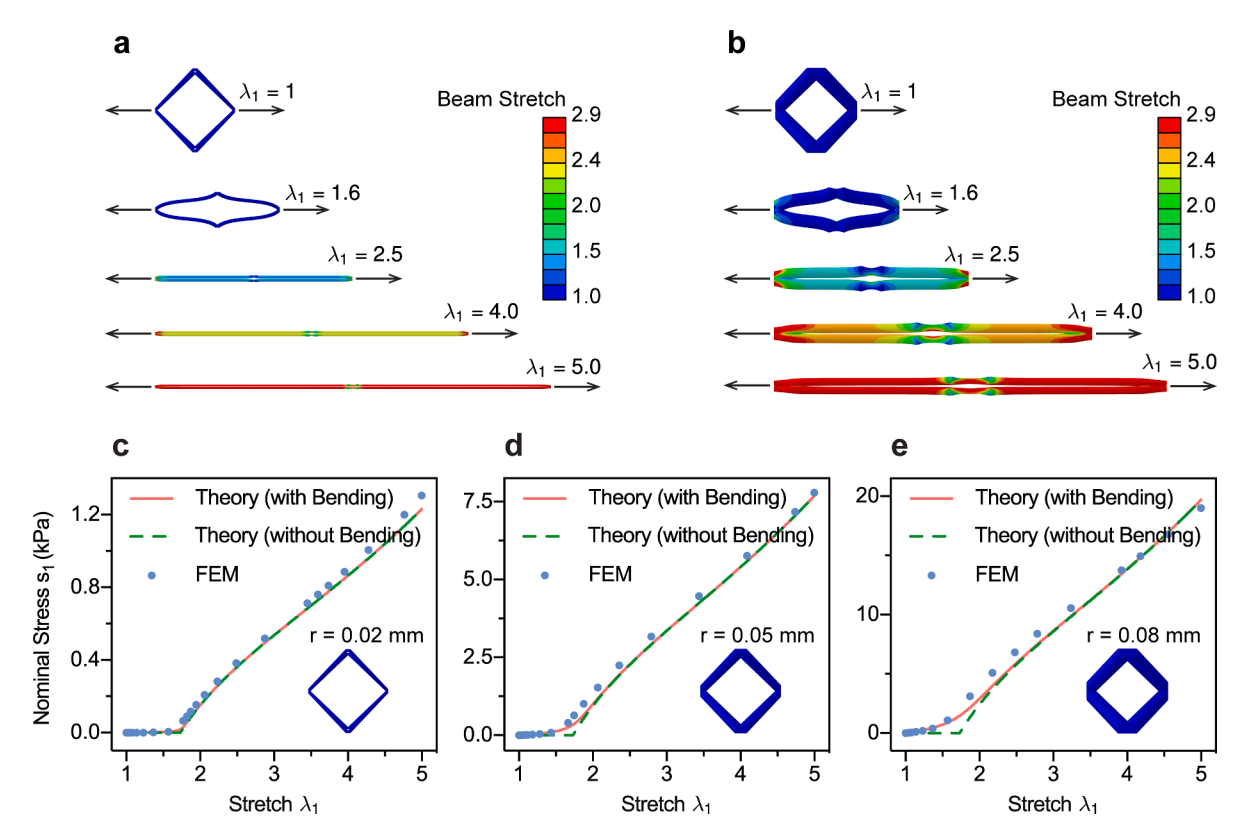


Fig. 10. Case studies for Octahedral lattices with different beam radii. (a-b) Contour plot of beam stretch with the sequential stretching process simulated with ABAQUS for (a) r = 0.02 mm, and (b) r = 0.08 mm. (c-e) FEM verification of stress-stretch with different beam radii (c) r = 0.02 mm, (d) r = 0.05 mm, and (e) r = 0.08 mm.

stress around the beam corner. To address this issue, we construct the theoretical models in two ways: with or without the bending model. In the low volume fraction case (r = 0.02 mm, Fig. 10c), the bending model does not produce a significant difference, and the individual stretching model is able to capture the stress-stretch behavior precisely. However, in the high volume fraction case (r = 0.08 mm, Fig. 10e), neglecting the bending model will compromise the accuracy, while the combination of stretching and bending models works better compared with FEM results. This verification demonstrates that the proposed model is able to address the mixed stretching-bending mechanism by superposing two separate models into a general framework.

4.4. Effects of lattice architectures

Next, the effect of the lattice architectures on the stress-stretch behaviors of elastomer lattices is discussed. Three lattice architectures are studied: Octet-truss (**Fig. 9a**), Rhombic (**Fig. 11a**), and Octahedral (**Fig. 11b**). The side length of the RVEs is 1 mm, and the beam radius is 0.05 mm (**Figs. 9a** and **11ab**). The CAD models of two RVEs are imported into ABAQUS for structural analysis with the Arruda-Boyce model. In the post-processing, the sequential stretching processes for lattice RVEs are demonstrated from the reference configuration to the current configuration (**Figs. 9b** and **11cd**). In **Fig. 11e**, three lattice architectures are modeled with the identical beam radius r = 0.05 mm, and the corresponding volume fraction for Octet-truss, Rhombic, and Octahedral lattices are calculated as 11.32%, 15.84%, and 4.92%, respectively. It is observed that the stiffness of lattice architecture increases with increasing volume fraction, because the high-volume fraction lattice results in high nominal stress under the same stretch.

In contrast, in the case study in Fig. 11f, three lattice architectures are modeled with identical volume fraction 4.92% (the volume fraction of Octahedral lattice used in Fig. 11b) but different beam radius. The volume is calculated in Solidworks, and the corresponding beam radii for Octet-truss, Rhombic, and Octahedral lattices are 0.0318 mm, 0.0265 mm, and 0.05 mm, respectively. As opposed to the case study of identical beam radius in Fig. 10e, three lattice architectures of identical volume fraction exhibit similar stress-stretch behavior over large deformation (i.e., stretch higher than 2.5). It is only during the small deformation region that the lattice architecture has a considerable impact on the stress-stretch behavior. This phenomenon could be described as that all lattice architectures are stretching-dominated over a large deformation, during which the beam members are uniaxially stretched with

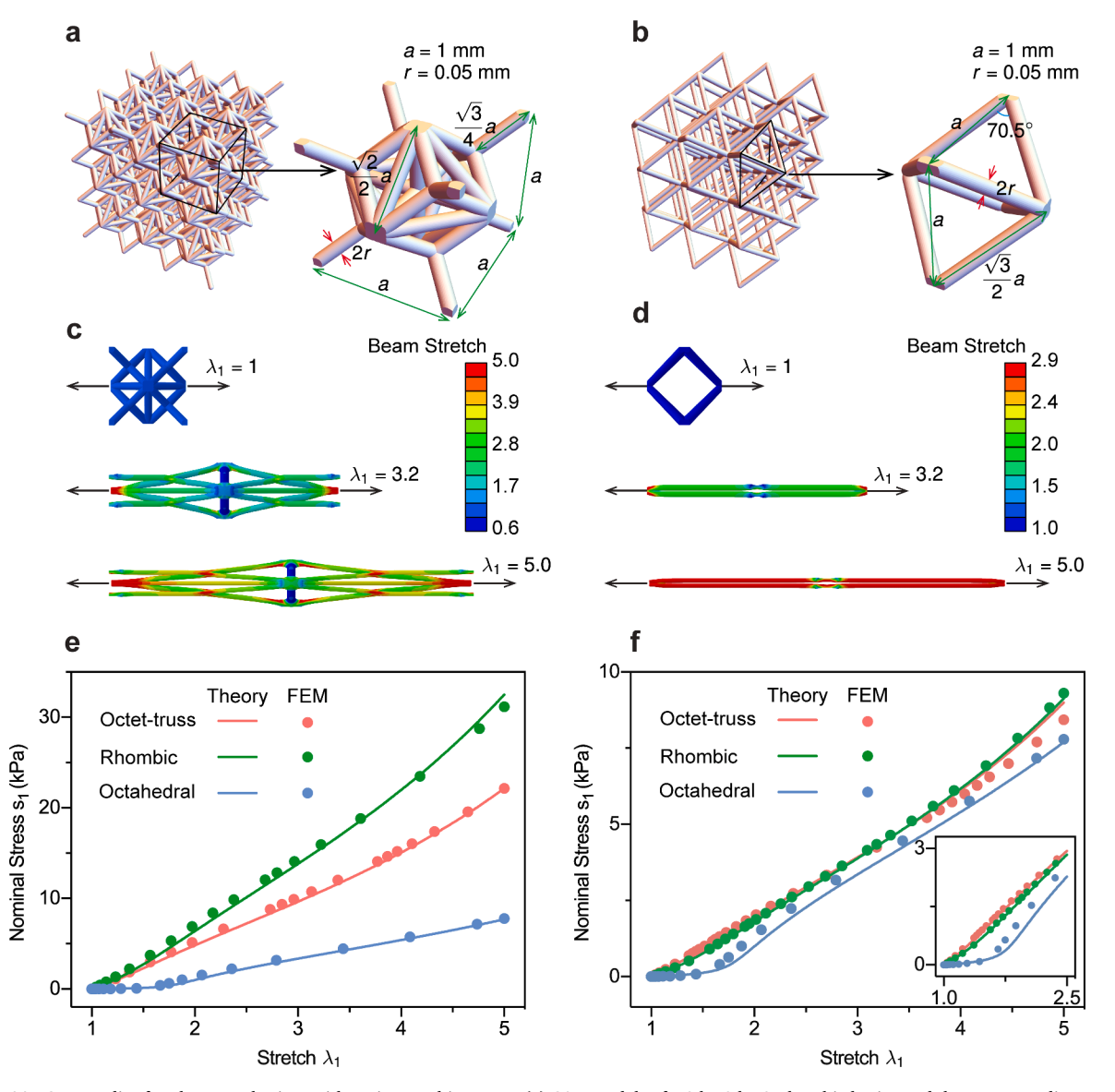


Fig. 11. Case studies for elastomer lattices with various architectures. (a) CAD models of a 3 by 3 by 3 Rhombic lattice and the corresponding RVE. (b) CAD models of a 3 by 3 by 3 Octahedral lattice and the corresponding RVE. (c) Contour plot of beam stretch with the sequential stretching process simulated with ABAQUS for Rhombic lattice. (d) Contour plot of beam stretch with the sequential stretching process simulated with ABAQUS for Octahedral lattice. (e) FEM verification of stress-stretch curves for three lattice architectures with identical beam radius r = 0.05 mm. (f) FEM verification of stress-stretch curves for three lattice architectures with identical volume fraction 4.92%.

negligible flexural behavior. During the relatively small deformation region, the ratios between stretching energy and total energy (stretching and bending) follow a sequence

$$\eta_{Octet} > \eta_{Rhombic} > \eta_{Octahedral}$$
 (49)

Therefore, the stress responses of the lattices follow a sequence Octet > Rhombic > Octahedral within the stretch of 1–2.5 (inset of Fig. 11f).

4.5. Effects of non-symmetric geometry and deformation

The numerical simulations in the previous sections mainly focus on the uniaxial stretching of symmetric lattices. This section will

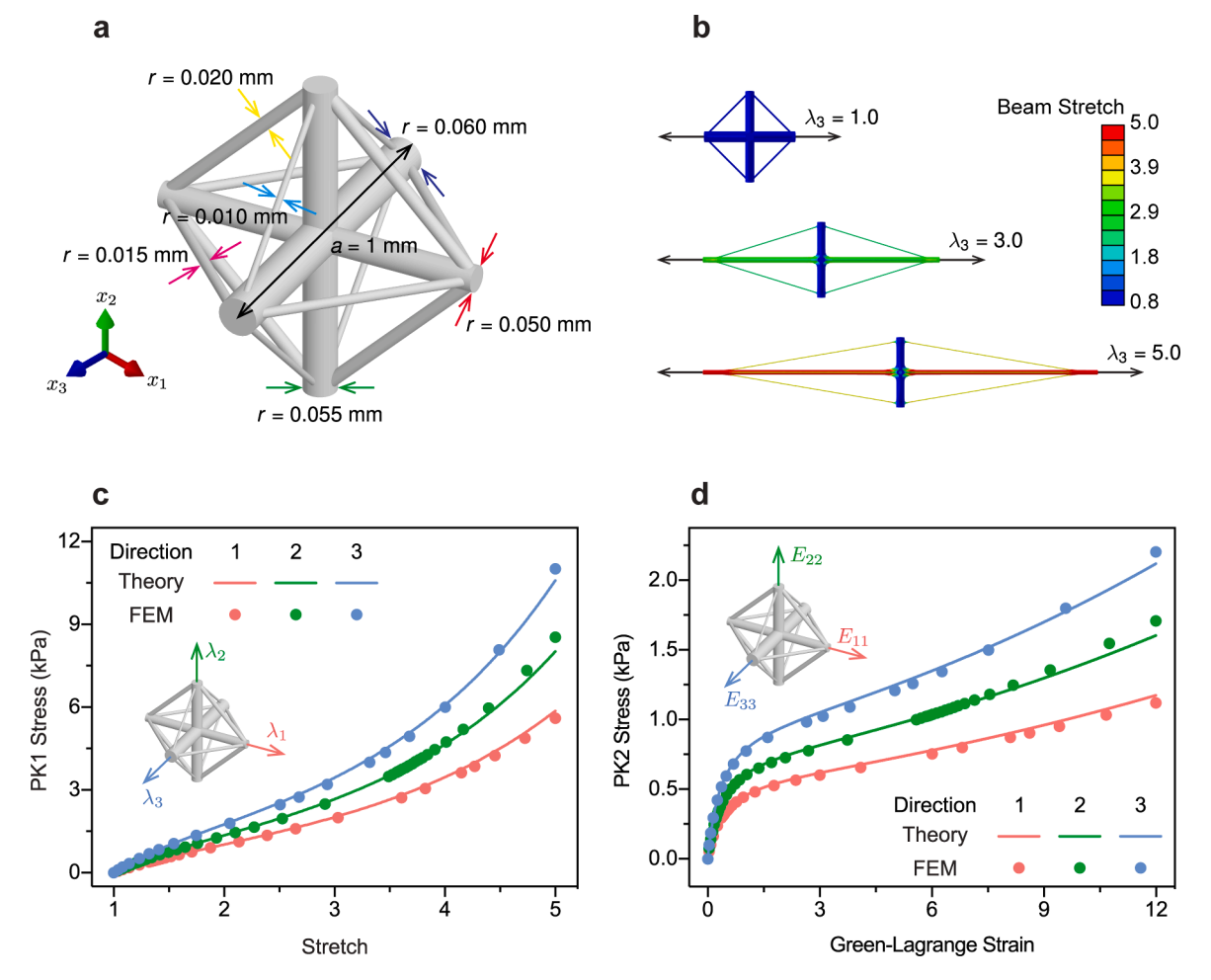


Fig. 12. Tension of a non-symmetric diamond lattice. (a) CAD models of the non-symmetric diamond lattice RVE. (b) Contour plot of beam stretch with the sequential stretching process simulated with ABAQUS. (c) Theoretical and numerical results of PK1 stress vs stretch curves in three loading directions. (d) Theoretical and numerical results of PK2 stress vs Green-Lagrange strain curves in three loading directions.

demonstrate that the proposed method is also capable of explaining the behaviors of elastomer lattices with non-symmetric geometries and under non-symmetric deformations.

In a general case, the deformation gradient is written as a superposition of stretching and shearing, as

$$\mathbf{F} = \frac{\partial \mathbf{x}}{\partial \mathbf{X}} = \begin{bmatrix} \lambda_1 & F_{12} & F_{13} \\ F_{21} & \lambda_2 & F_{23} \\ F_{31} & c_{32} & \lambda_3 \end{bmatrix}, \tag{50}$$

where λ_i denotes the stretch in the i^{th} direction, and $F_{ij} = \tan\theta_{ij}$ denotes the tangent of angle change θ_{ij} on the $x_i - x_j$ plane. Given the deformation gradient, the beam stretch $\hat{\lambda}$ is calculated via Eq. (4) as

$$\hat{\lambda} = \sqrt{\mathbf{N} \cdot \mathbf{C} \mathbf{N}} = \sqrt{\mathbf{N} \cdot \mathbf{F}^T \mathbf{F} \mathbf{N}}.$$
(51)

Without loss of the generality, a material constitutive model \widehat{W} associated with the first invariant of the right Cauchy-Green tensor \widehat{I}_1 is written as $\widehat{W} = \widehat{W}(\widehat{I}_1)$. Thus, the first Piola-Kirchhoff (PK1) stress for a beam is obtained via the work-conjugate relation and chain rule as

$$\widehat{\mathbf{P}} = \frac{\partial \widehat{W}}{\partial \mathbf{F}} = \frac{\mathrm{d}\widehat{W}}{\mathrm{d}\widehat{I}_{1}} \frac{\mathrm{d}\widehat{I}_{2}}{\mathrm{d}\widehat{\lambda}} \frac{\partial \widehat{\lambda}}{\partial \mathbf{F}} = 2\widehat{W}' (1 - \widehat{\lambda}^{-3}) \mathbf{F} \mathbf{N} \otimes \mathbf{N}, \tag{52}$$

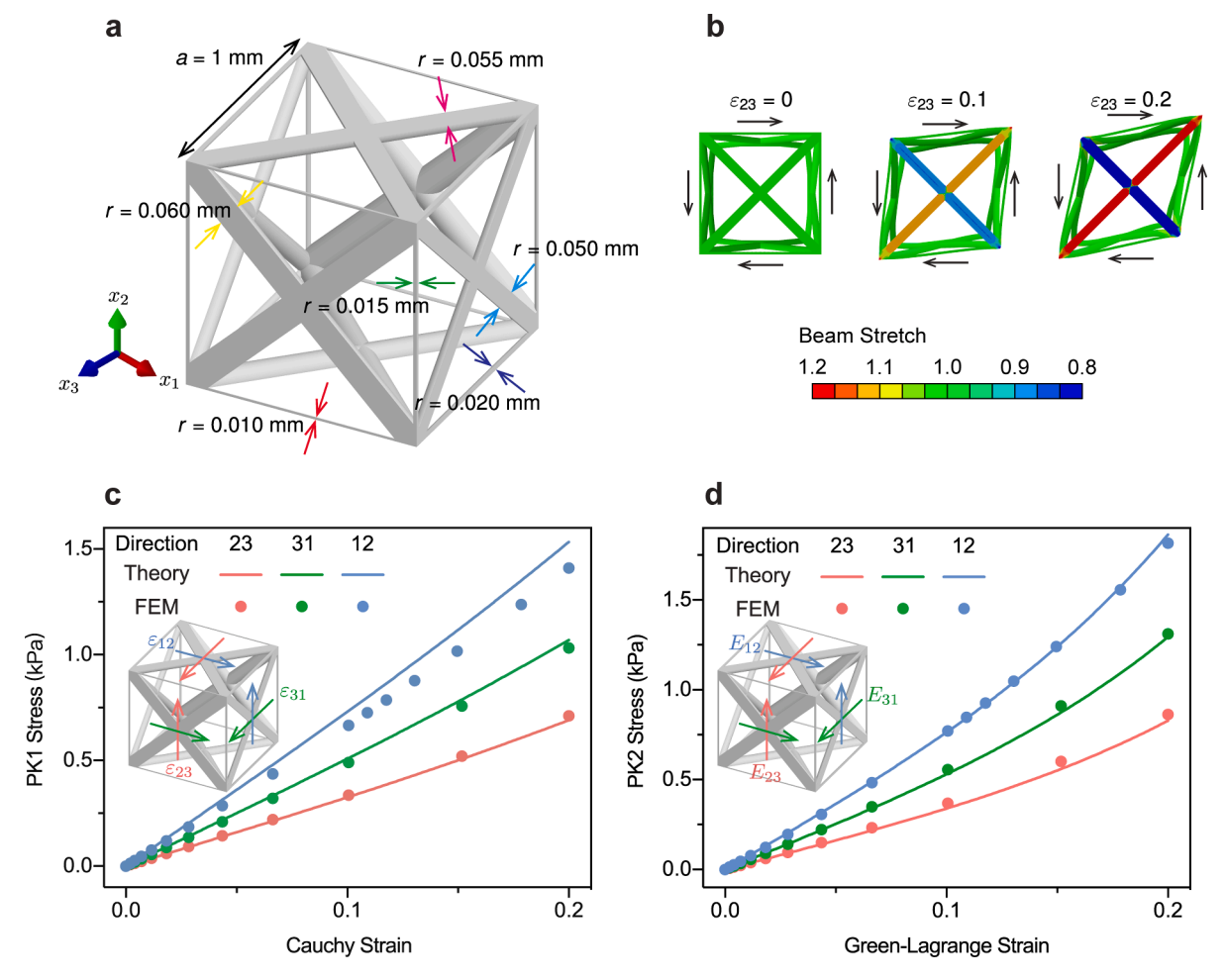


Fig. 13. Pure shear of an orthotropic cubic lattice. (a) CAD models of a cubic lattice RVE. (b) Contour plot of beam stretch with the sequential deformation process simulated with ABAQUS. (c) Theoretical and numerical results of PK1 stress vs Cauchy strain curves in three loading directions. (d) Theoretical and numerical results of PK2 stress vs Green-Lagrange strain curves in three loading directions.

where \widehat{W}' is the derivative of the strain energy function, and $\widehat{I}_1 = \widehat{\lambda}^2 - 2\widehat{\lambda}^{-1}$ in Eq. (14) is the first invariant of the right Cauchy-Green tensor featuring the uniaxial stretch along the beam axial direction.

The above homogenization could be applied to other stress and strain measures. For instance, the Green-Lagrange strain is expressed as

$$\mathbf{E} = \frac{1}{2} \left(\mathbf{F}^{\mathsf{T}} \mathbf{F} - \mathbf{I} \right) = \frac{1}{2} (\mathbf{C} - \mathbf{I}). \tag{53}$$

The beam stretch $\hat{\lambda}$ in Eq. (51) is written with respect to the Green-Lagrange strain E as

$$\widehat{\lambda} = \sqrt{2\mathbf{N} \cdot \mathbf{E} \mathbf{N} + 1}.$$

Thus, the second Piola-Kirchhoff (PK2) stress for a beam is obtained via the work-conjugate relation as

$$\widehat{\mathbf{T}} = \frac{\partial \widehat{W}}{\partial \mathbf{E}} = \frac{\mathrm{d}\widehat{W}}{\mathrm{d}\widehat{I}_{1}} \frac{\mathrm{d}\widehat{I}_{1}}{\mathrm{d}\widehat{\lambda}} \frac{\partial \widehat{\lambda}}{\partial \mathbf{E}} = 2\widehat{W}' (1 - \widehat{\lambda}^{-3}) \mathbf{N} \otimes \mathbf{N}.$$
(55)

The stress-strain relations have been established in different measures, as indicated in Eqs. (52) and 55. In the following subsections, we will study the tensile deformation of a non-symmetric diamond lattice (Section 4.5.1) and the shear deformation of an orthotropic cubic lattice (Section 4.5.2).

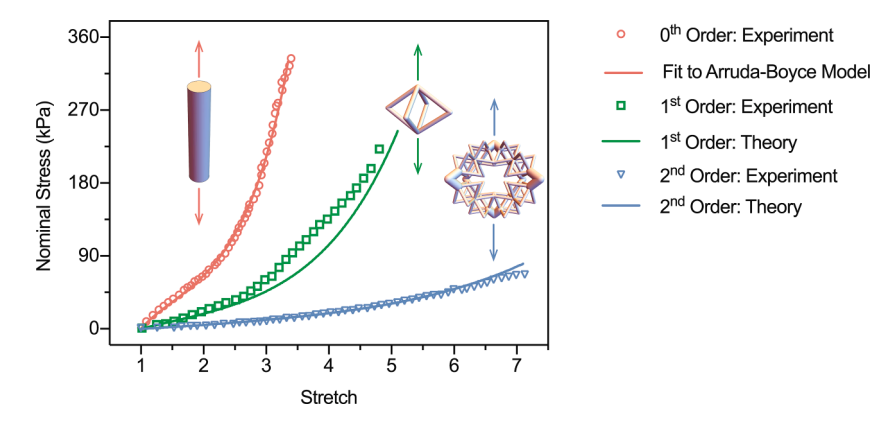


Fig. 14. Experimental validation of stress-stretch curves for hierarchical Octahedral lattices.

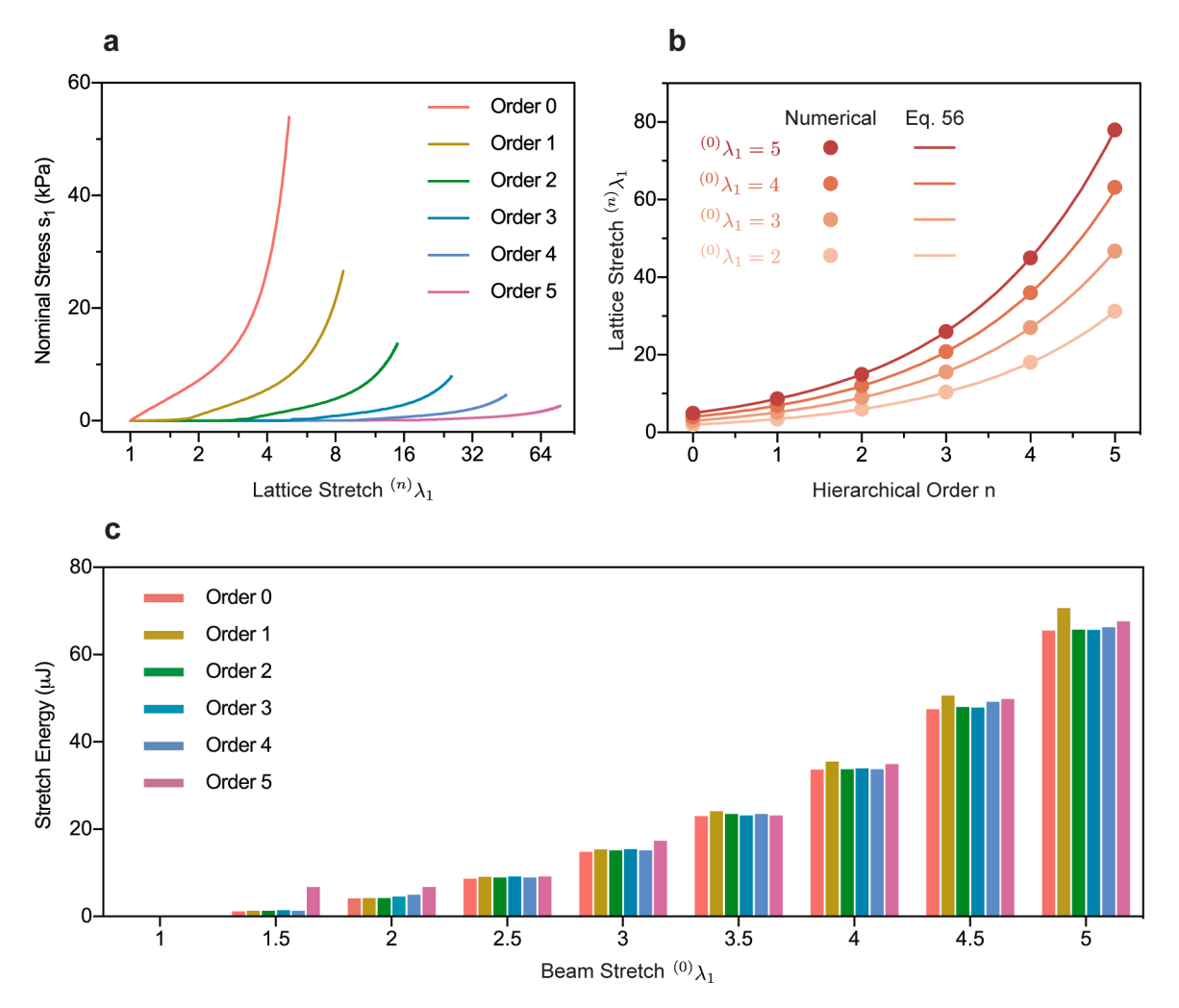


Fig. 15. Case studies of hierarchical elastomer lattices. (a) Stress-stretch curves for various hierarchical order elastomer lattices; (b) The global lattice stretch corresponding to different beam stretch for various hierarchical order; (c) The stretching energy of different hierarchical order lattice under various beam stretch.

4.5.1. Tension of a non-symmetric diamond lattice

In this section, a non-symmetric diamond lattice is presented with different beam diameters in each direction. The CAD model and geometry details are illustrated in Fig. 12a, and the simulated sequential stretching processes for diamond lattice RVE are demonstrated from the reference configuration to the current configuration in Fig. 12b. The comparisons between the FEM simulation and theoretical modeling of PK1 stress vs stretch and PK2 stress vs Green-Lagrange strain are illustrated in Figs. 12cd, respectively. Because the beam diameter in the x_1 direction is the smallest and in the x_3 direction is the largest, the stiffness also follows the sequence as $P_{11} < P_{22} < P_{33}$ and $T_{11} < T_{22} < T_{33}$. As shown in Figs. 12cd, our theoretical modeling results agree well with the FEM results of the stress-strain behaviors of this non-symmetric lattice.

4.5.2. Pure shear of an orthotropic cubic lattice

In this section, an orthotropic cubic lattice under pure shear deformation is studied. The CAD model and geometry details are illustrated in **Fig. 13a**, and the simulated sequential deformation processes for cubic lattice RVE are demonstrated from the reference configuration to the current configuration in **Fig. 13b**. By eliminating the rigid body rotation, the shear components of the deformation gradient coincide with the Cauchy strain as $F_{ij} = \varepsilon_{ij}$. The comparisons between the FEM simulation and theoretical modeling of PK1 stress vs Cauchy strain and PK2 stress vs Green-Lagrange strain are illustrated in **Figs. 13cd**, respectively. Because the beam diameter on the $x_2 - x_3$ plane is the smallest and in the $x_1 - x_2$ plane is the largest, the stiffness also follows the sequence as $P_{23} < P_{31} < P_{12}$ and $T_{23} < T_{31} < T_{12}$. It is observed that the theoretical model could accurately predict the stress-strain behavior by comparing with FEM results (**Figs. 13cd**).

4.6. Effects of hierarchical orders

The theoretical model has been verified for the first-order lattice architectures in Sections 4.2 to 4.5. This section will focus on the theoretical modeling and experimental verification for hierarchical Octahedral lattices. The previous study demonstrated the fabrication and experimental testing of hierarchical lattices (Li et al., 2017), and their experimentally measured stress-stretch curves will be compared with our theoretical model. First, the data collected from the stress-stretch curve for the 0^{th} order lattice is fitted to the Arruda-Boyce model to obtain the material constants as $\mu_0 = 22.50$ kPa and $\lambda_m = 1.69$. Then, the theoretically predicted stress-stretch curves are obtained with the above-mentioned MATLAB algorithm and compared with the experimental data, which are illustrated in Fig. 12. It is observed that the bulk material, which is considered the 0^{th} order structure, ruptures when stretch reaches 3.5. With the aid of enhanced flexibility in higher-order lattice, the lattice ruptures at $\lambda \approx 5$ for the first order lattice and $\lambda \approx 7.1$ for the second-order lattice.

Limited by the manufacturing technique, it is challenging to have high-order lattice order lattice realized and tested experimentally, especially for the order higher than three. Nevertheless, exploring the mechanical behavior of fractal-like multiscale lattice is still of interest to both engineers and researchers. Therefore, the algorithm mentioned in Section 3.5 is applied to the 0^{th} , 1^{st} , 2^{nd} , 3^{rd} , 4^{th} , 5^{th} order lattice. The material property is given in Table 1 (with the Arruda-Boyce model). The geometry information of the 1^{st} order lattice is illustrated in Fig. 11b. It is assumed that each order has the identical material property and volume fraction. The algorithm is looped with incremental applied stress s_1 until the local beam stretch reaches ${}^{(0)}\lambda_1=5$, at which we assume the material rupture and thus terminate the iteration. The stress-stretch curves for various orders lattice are illustrated in Fig. 15a, which is in accordance with the statement that the higher-order is more compliant and gradually reduces to zero stiffness. Note that the x-y axis in Fig. 15a is $\log_2 v_3$ linear.

During the stretching process, the Octahedral lattice exhibits a positive effective Possion's ratio. Namely, ${}^{(i)}\lambda_2$, ${}^{(i)}\lambda_3 < 1$ when ${}^{(i)}\lambda_1 > 1$. Moreover, it is noted in Fig. 10 that the lattice will contract in the lateral direction and thus the cross-sectional area almost collapses to zero when subjected to a large stretch, which is mathematically written as ${}^{(i)}\lambda_2$, ${}^{(i)}\lambda_3 \approx 0$. Therefore, the kinematic compatibility condition in Eq. 29 can be approximated as

$$^{(n)}\lambda_1 \approx 3^{\frac{n}{2}(0)}\lambda_1,$$
 (56)

which states that the relation between global lattice stretch $^{(n)}\lambda_1$ and local beam stretch $^{(0)}\lambda_1$ can be approximated as a power function. This relation is also a reference to verify the accuracy of the numerical results presented in **Section 3.5**. In the case studies, we choose the beam stretch $^{(0)}\lambda_1=2$, 3, 4, 5 as four different cases. To reach the given beam stretch $^{(0)}\lambda_1$, each hierarchical order lattice corresponds to a different global lattice stretch $^{(n)}\lambda_1$. The global lattice stretch $^{(n)}\lambda_1$ is plotted as a function of lattice hierarchical order n under various given beam stretches $^{(0)}\lambda_1$ in **Fig. 15b**, where the numerical results from MATLAB simulation and theoretical prediction in Eq. 56 are presented. It is observed that, under a given beam stretch, the higher-order lattice exhibits more compliance, and the numerical results match well with the proposed theoretical calculations in Eq. 56.

In addition, because the material property and volume fraction are identical in each hierarchical order lattice, the stretching strain energy for each hierarchical order lattice should be identical under the same beam stretch $^{(0)}\lambda_1$. This is a useful criterion to verify the feasibility and accuracy of the proposed numerical algorithm. The stretching energy of 0^{th} order lattice is calculated via Eq. 11, which can be used to compare with the stretching energy of high-order lattice. The stretching energy is plotted as a function as beam stretch for lattice hierarchical order ranging from 0 to 5 in Fig. 15c, where the 0^{th} order lattice energy is obtained analytically via the Arruda-

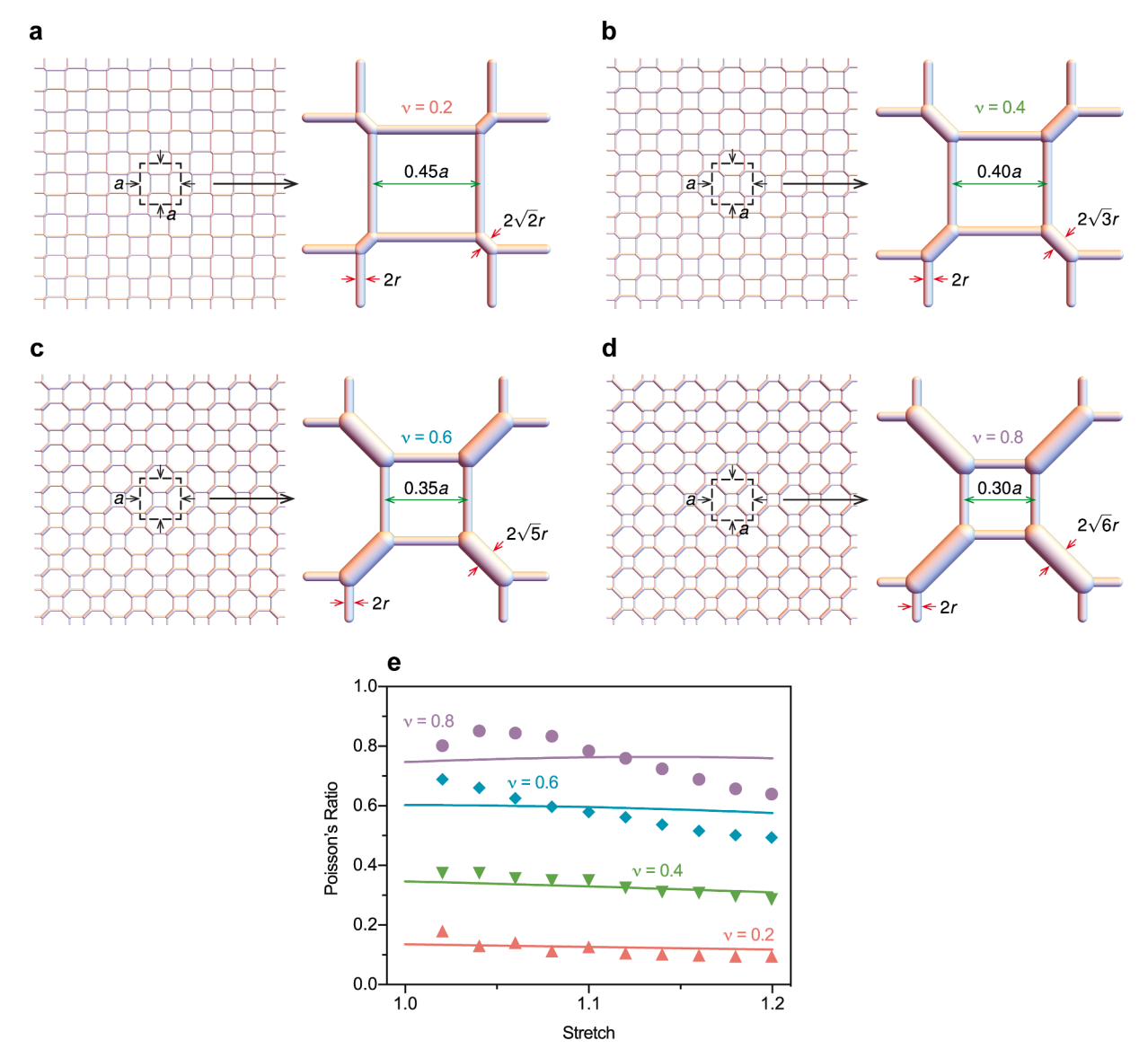


Fig. 16. Using the proposed theoretical model to explain Poisson's ratios. (a-d) Schematic illustration of lattice architectures and the corresponding RVE geometry for (a) $\nu=0.2$, (b) $\nu=0.4$, (c) $\nu=0.6$, and (d) $\nu=0.8$. (e) The comparison between the experimentally measured Poisson's ratios and theoretically calculated results.

Boyce model in Eq. 5, and other higher-order lattice energy is obtained numerically via the nonlinear optimization algorithm in MATLAB.

Note that the results for high-order hierarchical lattices shown in Fig. 15 are theoretical predictions that may inspire future experimental investigations. For 2D hierarchical lattices, the existing studies showed structures with the 4th hierarchical order (Ajdari et al., 2012; Haghpanah et al., 2013; Mousanezhad et al., 2015; Oftadeh et al., 2014a; Oftadeh et al., 2014b). However, for 3D hierarchical lattices, the existing studies only demonstrated structures with the 3rd hierarchical order (Li et al., 2017; Meza et al., 2015; Zheng et al., 2016). More explorations for 3D lattices with higher hierarchical orders are needed in the future research.

4.7. Study Poisson's ratio of elastomer metamaterials

To further verify the capability of the proposed theoretical model, we show a case study using the proposed theory to calculate the Poisson's ratios of elastomer metamaterials. Inspired by Origami and Kirigami, a large number of metamaterials are designed and

manufactured with remarkable and designated mechanical properties (An et al., 2020; Lin et al., 2020). With the aid of topology optimization, previous research reported that a programmable lattice could be designed with an effective Poisson's ratio ranging from -0.8 to 0.8 (Clausen et al., 2015; Wang et al., 2014). We herein choose four cases and use a network of straight beams to approximate their spiral beam members, with $\nu = 0.2$, $\nu = 0.4$, $\nu = 0.6$, and $\nu = 0.8$, respectively. The schematic illustration of four lattice architectures and the corresponding RVEs is demonstrated in Figs. 16a to d. The comparison of Poisson's ratio between the proposed theoretical model and experimental data in the literature is demonstrated in Fig. 16e. Results in Fig. 16e demonstrate that our theoretical model of the elastomer lattice can explain the Poisson's ratios of the experimentally fabricated elastomer metamaterials in others' works (Clausen et al., 2015; Wang et al., 2014).

5. Concluding remarks

This paper presents a theoretical framework to understand the stress-stretch behavior for elastomer lattices over large deformation. In order to theoretically understand the mechanics of lattices, two distinct deformation models are considered, including the stretching and bending modes during the deformation. The stretching is described by the axial elongation of beam ligaments, while the bending is characterized by the rotation of beam ligaments. Both axial elongation and rotation can be associated and obtained with the deformation gradient of the macroscopic lattice. The potential energy function for the lattice RVE is constructed regarding the two deformation modes and is decomposed into stretching energy and bending energy. The proposed theory is then followed by a general model for hierarchical lattices. According to the principle of virtual work, the generalized forces in a deformable continuum are obtained. The minimum strain energy can be found with the aid of a nonlinear optimization algorithm. Having been theoretically analyzed and numerically implemented in MATLAB, several case studies are performed and compared with FEM results and experimental data in the literature. The accuracy of the theoretical model has been verified with high-fidelity simulations in ABAQUS. The comparisons demonstrate that the model is capable of describing the stress-stretch behavior for lattices with various material constitutive models, volume fractions, and lattice architectures, which successfully confirm the accuracy and robustness of the proposed model. The predictions for hierarchical lattices and programmable metamaterials also match with the existing experiments in the literature.

The highlight of this research work is that it provides an analytical tool to quantify the stretching and bending behaviors for elastomer lattices over large deformation. With this model, the mechanical performance of stretchy elastomer lattices is theoretically understood and characterized. Furthermore, this work presents a framework for hierarchical lattices based on generalized coordinates and generalized forces in analytical dynamics. Therefore, this mechanical problem is converted to a geometry problem in a higher dimensional Riemann space. Without doing cumbersome hand calculations, a non-linear optimization algorithm is incorporated to find the minimum potential energy subjected to holonomic constraints. From a more in-depth perspective, this procedure is identically considered as looking for a geodesic in the configuration space. Overall, this work proposes an accurate and robust theoretical framework to predict the mechanical behavior of lattice structures with the minimum computational cost. This work is not limited to analyzing the existing lattice architectures but also has the potential of designing and predicting metamaterials toward the desired criterion.

The key idea of the proposed model is motivated by the polymer networks. In the polymer network scale, the free energy of one polymer chain is written in terms of a probability density function (Rubinstein and Colby, 2003; Treloar, 1975). Take the Arruda-Boyce model as an example (Arruda and Boyce, 1993), the free energy of the polymer chain is described with the Langevin chain model, and the connection between the macroscale deformation and the microscale chain stretch is established using a body-centered cubic structure. In the lattice model in this paper, if the stretching energy of the beam is also described by Langevin model and the bending energy is removed, our model should be equivalent to the Arruda-Boyce model.

Despite the great features, this model may not be suitable for capturing some complex behaviors, such as snap-through, snap-back, buckling, and fractures, which apparently do not follow the affine deformation pattern. Besides, because this theory is modeled with one-dimensional structural beam members, it focuses on the global force-displacement behavior but cannot address the stress distribution and concentration around complex joint areas.

Credit author statement

Yanchu Zhang: Conceptualization, Methodology, Software, Validation, Formal analysis, Investigation, Resources, Writing, Visualization. Kunhao Yu: Methodology, Investigation, Resources, Writing. Kyung Hoon Lee: Investigation, Resources. Ketian Li: Investigation, Resources. Haixu Du: Investigation, Resources. Qiming Wang: Conceptualization, Methodology, Formal analysis, Resources, Writing, Visualization, Supervision, Funding acquisition.

CRediT authorship contribution statement

Yanchu Zhang: Conceptualization, Methodology, Software, Validation, Formal analysis, Investigation, Resources, Visualization. Kunhao Yu: Methodology, Investigation, Resources. Kyung Hoon Lee: Investigation, Resources. Ketian Li: Investigation, Resources.

Haixu Du: Investigation, Resources. Qiming Wang: Conceptualization, Methodology, Formal analysis, Resources, Visualization, Supervision, Funding acquisition.

Declaration of Competing Interest

The authors declare that they have no known competing financial interests or personal relationships that could have appeared to influence the work reported in this paper.

Acknowledgments

We acknowledge the funding support from the Air Force Office of Scientific Research (FA9550–18–1–0192), the National Science Foundation (CMMI-1762567 and CMMI-1943598), and the Office of Naval Research Young Investigator Program.

Appendix A. Hyperelastic Constitutive Models

The strain energy functions and nominal stress-stretch behaviors of the elastomer under plane-stress tension are given in the section. The strain energy of the neo-Hookean model is written as

$$W(\lambda_1, \lambda_2, \lambda_3) = \frac{\mu}{2} \left(\lambda_1^2 + \lambda_2^2 + \lambda_2^2 - 3 \right), \tag{A-1}$$

where λ_1 , λ_2 , and λ_3 are three principal stretches, and μ is the shear modulus. The nominal stress-stretch of an incompressible elastomer under uniaxial tension is derived as

$$s = \mu(\lambda - \lambda^{-2}),$$
 (A-2)

where *s* is the nominal stress and λ is the uniaxial stretch.

The strain energy of the first-order Ogden model is written as

$$W(\lambda_1, \lambda_2, \lambda_3) = \frac{2\mu_1}{\alpha_1^2} (\lambda_1^{\alpha_1} + \lambda_2^{\alpha_1} + \lambda_2^{\alpha_1} - 3), \tag{A-3}$$

where μ_1 and α_1 are two parameters. The nominal stress-stretch of an incompressible elastomer under plane-stress tension is derived as

$$s = \frac{\mu_1}{\alpha_1} \left(\lambda_1^{\alpha_1 - 1} - \lambda_1^{-\frac{\alpha_1}{2} - 1} \right) \tag{A-4}$$

The strain energy of the Arruda-Boyce model is approximated by Taylor expansion, which is written as

$$W(\lambda_1, \lambda_2, \lambda_3) = \mu \left[\frac{1}{2} (I_1 - 3) + \frac{1}{20\lambda_m^2} (I_1^2 - 9) + \frac{11}{1050\lambda_m^4} (I_1^3 - 27) \right], \tag{A-5}$$

where $I_1 = \lambda_1^2 + \lambda_2^2 + \lambda_3^2$ and λ_m is the parameter to indicate the limiting stretch. The nominal stress-stretch of an incompressible elastomer under uniaxial tension is derived as

$$s = \mu \left(\lambda_1 - \lambda_1^{-2}\right) \left(1 + \frac{I_1}{5\lambda_m^2} + \frac{11I_1^2}{175\lambda_m^4}\right). \tag{A-6}$$

Appendix B. Validation of the Affine Deformation Assumption

The kinematic analysis presented in the theoretical model postulates an affine deformation of the unit cell. Namely, the deformation of the beam ligament follows the same pattern as the homogenized unit cell. Given a deformation gradient applied upon the unit cell, the stretch and direction of a beam ligament can be fully determined via Eqs. (4)-5, respectively. In order to check the validity of the affine deformation assumption, the stretch $\hat{\lambda}$ and the directional cosine vector \mathbf{n} of representative beams are computed analytically and compared with FEM results.

For a representative beam ligament with two ends denoted by nodes A and B, the nodal location vectors of A and B during the deformation are extracted from ABAQUS as \mathbf{x}_A and \mathbf{x}_B . Therefore, the stretch $\widehat{\lambda}$ and directional cosine vector \mathbf{n} are numerically

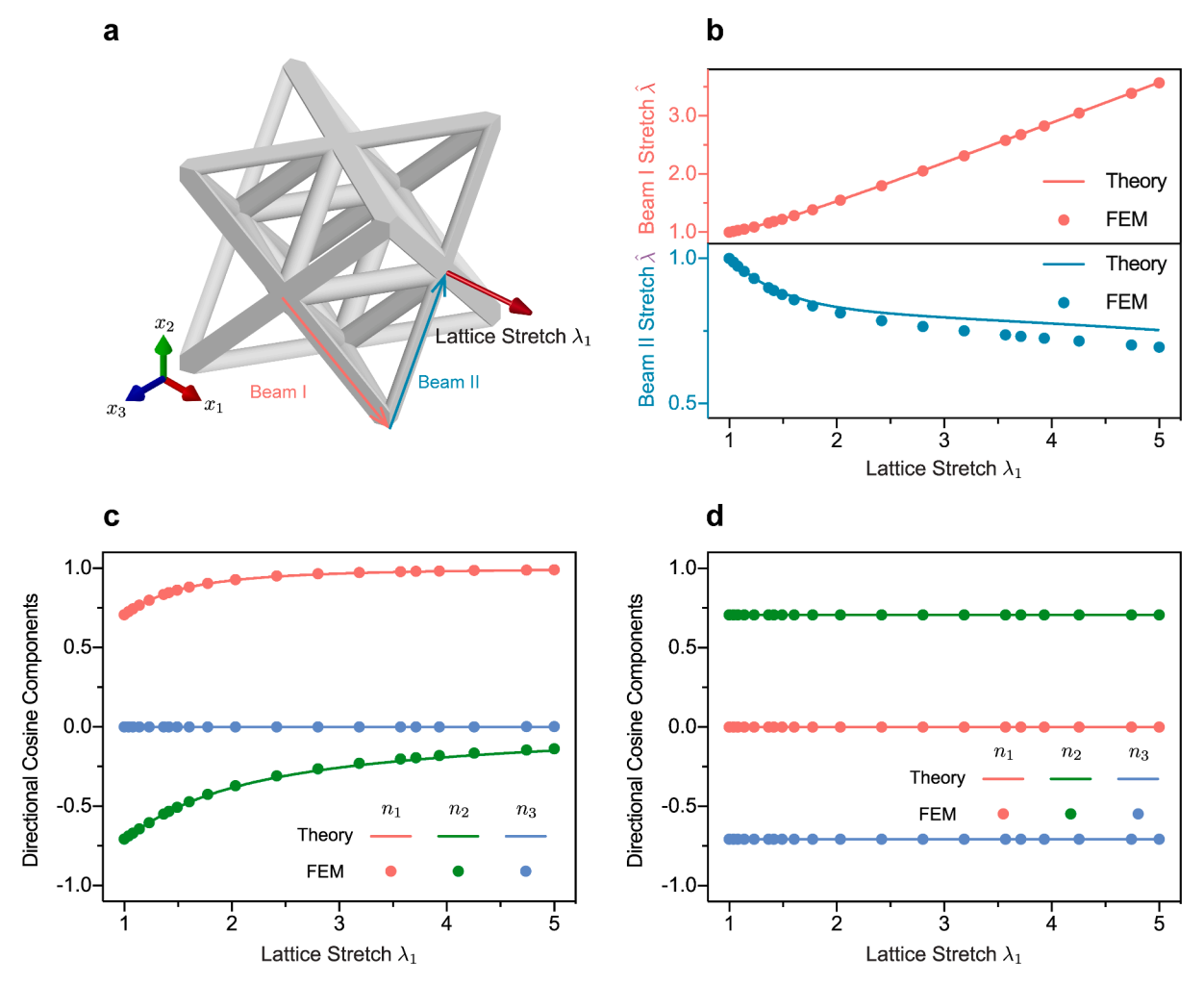


Fig. B1. Verification of the affine deformation assumption for the Octet-truss lattice. (a) CAD model of an Octet-truss unit cell and two representative beams. (b) Verification of stretch $\hat{\lambda}$ of beams I and II. (c) Verification of directional cosine vector components for beam I. (d) Verification of directional cosine vector components for beam II.

calculated as

$$\widehat{\lambda} = \frac{l}{L} = \frac{|\mathbf{x}_B - \mathbf{x}_A|}{L}.$$
(B-1)

$$\mathbf{n} = \frac{\mathbf{x}_B - \mathbf{x}_A}{|\mathbf{x}_B - \mathbf{x}_A|}.$$
 (B-2)

The numerical results in Eqs. B-1 and B-2 are obtained from ABAQUS and used to verify the analytical results in Eqs. (4)-5. The following efforts will focus on the validation of three different lattice architectures: Octet-truss lattice (Fig. B1), Rhombic lattice (Fig. B2), and Octahedral lattice (Fig. B3).

- **B.1 Octet-truss Lattice**
- **B.2** Rhombic Lattice
- **B.3 Octahedral Lattice**

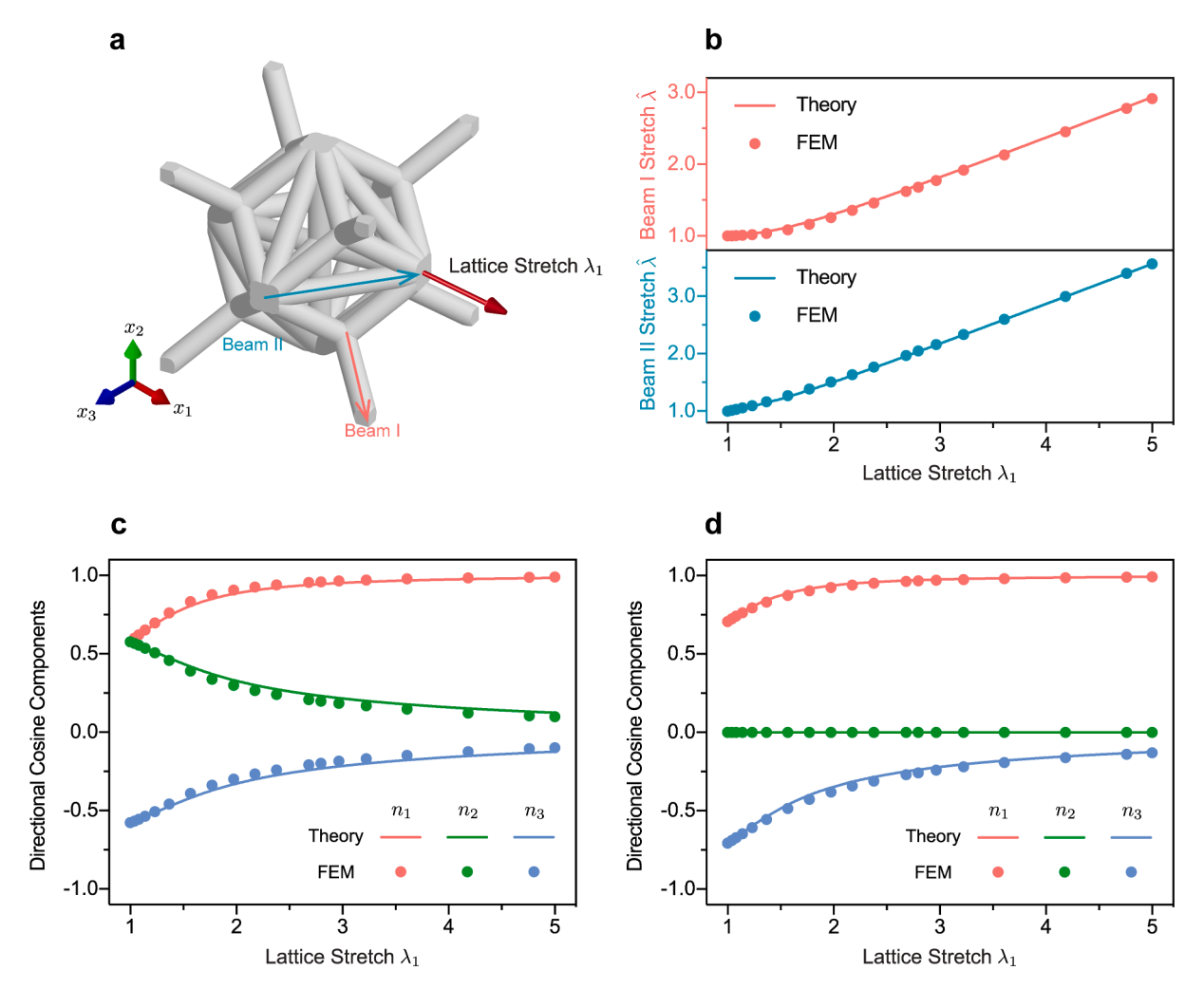


Fig. B2. Verification of the affine deformation assumption for the Rhombic lattice. (a) CAD model of a Rhombic unit cell and two representative beams. (b) Verification of stretch $\hat{\lambda}$ of beams I and II. (c) Verification of directional cosine vector components for beam I. (d) Verification of directional cosine vector components for beam II.

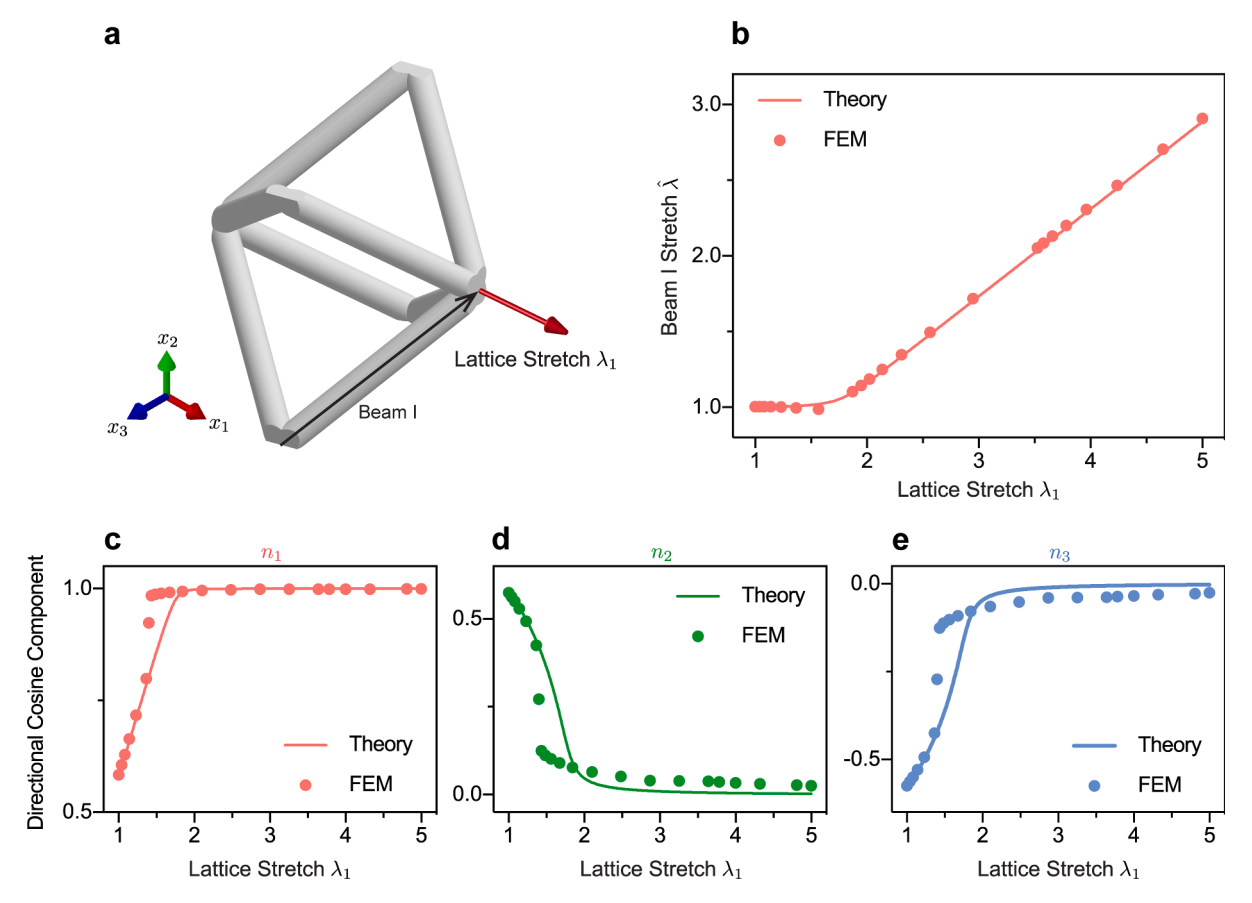


Fig. B3. Verification of the affine deformation assumption for the Octahedral lattice. (a) CAD model of an Octahedral unit cell and a representative beam. (b) Verification of stretch $\hat{\lambda}$ of beams I and II. (c-e) Verification of directional cosine vector components (c) n_1 , (d) n_2 , and (e) n_3 .

Appendix C. Potential Energy Function for Lattice Structures

In Section 3, we only present the potential energy function for an Octahedral lattice with the Arruda-Boyce model. The potential energy functions for other lattice architectures coupling various constitutive models are given as follows.

C.1. Octet-truss Lattice

• With neo-Hookean model:

$$W(\lambda_1, \lambda_2, \lambda_3) = \frac{\pi r^2}{\sqrt{2}a^2} \frac{\mu_0}{2} \left[8\lambda_1^2 + 8\lambda_2^2 + 8\lambda_3^2 + \frac{32}{\sqrt{2\lambda_1^2 + 2\lambda_2^2}} + \frac{32}{\sqrt{2\lambda_2^2 + 2\lambda_3^2}} + \frac{32}{\sqrt{2\lambda_3^2 + 2\lambda_1^2}} - 72 \right].$$
 (C-1)

• With Ogden model:

$$W(\lambda_{1}, \lambda_{2}, \lambda_{3}) = \frac{\pi r^{2}}{\sqrt{2}a^{2}} \sum_{p=1}^{N} \frac{2\mu_{p}}{\alpha_{p}^{2}} \left[8\left(\frac{1}{2}\lambda_{1}^{2} + \frac{1}{2}\lambda_{2}^{2}\right)^{\frac{a_{p}}{2}} + 8\left(\frac{1}{2}\lambda_{2}^{2} + \frac{1}{2}\lambda_{3}^{2}\right)^{\frac{a_{p}}{2}} + 8\left(\frac{1}{2}\lambda_{3}^{2} + \frac{1}{2}\lambda_{1}^{2}\right)^{\frac{a_{p}}{2}} + 16\left(\frac{1}{2}\lambda_{1}^{2} + \frac{1}{2}\lambda_{2}^{2}\right)^{-\frac{a_{p}}{4}} + 16\left(\frac{1}{2}\lambda_{2}^{2} + \frac{1}{2}\lambda_{3}^{2}\right)^{-\frac{a_{p}}{4}} + 16\left(\frac{1}{2}\lambda_{3}^{2} + \frac{1}{2}\lambda_{1}^{2}\right)^{-\frac{a_{p}}{4}} - 72\right].$$
(C-2)

• With Arruda-Boyce model:

Y. Zhang et al.

$$W(\lambda_{1}, \lambda_{2}, \lambda_{3}) = \frac{\pi r^{2}}{\sqrt{2}a^{2}} \mu_{0} \left(\frac{1}{2} \left[+32(2\lambda_{1}^{2} + 2\lambda_{2}^{2})^{-1/2} + 32(2\lambda_{2}^{2} + 2\lambda_{3}^{2})^{-1/2} + 32(2\lambda_{3}^{2} + 2\lambda_{1}^{2})^{-1/2} \right] + 32(2\lambda_{1}^{2} + 2\lambda_{2}^{2})^{-1/2} + 32(2\lambda_{2}^{2} + 2\lambda_{3}^{2})^{-1/2} + 32(2\lambda_{3}^{2} + 2\lambda_{1}^{2})^{-1/2} \right] + \frac{1}{20\lambda_{m}^{2}} \left[4\lambda_{1}^{4} + 4\lambda_{2}^{4} + 4\lambda_{3}^{4} + 4\lambda_{1}^{2}\lambda_{2}^{2} + 4\lambda_{2}^{2}\lambda_{3}^{2} + 4\lambda_{3}^{2}\lambda_{1}^{2} + 16(2\lambda_{3}^{2} + 2\lambda_{1}^{2})^{1/2} + 16(2\lambda_{2}^{2} + 2\lambda_{3}^{2})^{1/2} + 16(2\lambda_{3}^{2} + 2\lambda_{1}^{2})^{-1} + 64(2\lambda_{1}^{2} + 2\lambda_{2}^{2})^{-1} + 64(2\lambda_{2}^{2} + 2\lambda_{3}^{2})^{-1} + 64(2\lambda_{3}^{2} + 2\lambda_{1}^{2})^{-1} - 216 \right] + \frac{11}{1050\lambda_{m}^{4}} \left[2\lambda_{1}^{6} + 2\lambda_{2}^{6} + 2\lambda_{3}^{6} + 3\lambda_{1}^{4}\lambda_{2}^{2} + 3\lambda_{1}^{2}\lambda_{2}^{4} + 3\lambda_{2}^{4}\lambda_{3}^{2} + 3\lambda_{2}^{2}\lambda_{3}^{4} + 3\lambda_{3}^{4}\lambda_{1}^{2} + 3\lambda_{3}^{2}\lambda_{1}^{4} + 6(2\lambda_{1}^{2} + 2\lambda_{2}^{2})^{-3/2} + 6(2\lambda_{2}^{2} + 2\lambda_{3}^{2})^{-3/2} + 6(2\lambda_{3}^{2} + 2\lambda_{1}^{2})^{-3/2} + 512(2\lambda_{3}^{2} + 2\lambda_{1}^{2})^{-3/2$$

C.2. Rhombic Lattice

• With neo-Hookean model:

$$W(\lambda_{1}, \lambda_{2}, \lambda_{3}) = \frac{\pi r^{2}}{\sqrt{2}a^{2}} \frac{\mu_{0}}{2} \left(4\lambda_{1}^{2} + 4\lambda_{2}^{2} + 4\lambda_{3}^{2} + \frac{16}{\sqrt{2\lambda_{1}^{2} + 2\lambda_{2}^{2}}} + \frac{16}{\sqrt{2\lambda_{2}^{2} + 2\lambda_{3}^{2}}} + \frac{16}{\sqrt{2\lambda_{3}^{2} + 2\lambda_{1}^{2}}} - 36 \right)$$

$$+ \frac{\sqrt{3}\pi r^{2}}{2a^{2}} \frac{\mu_{0}}{2} \left[16\left(\frac{I_{1}}{3}\right) + 32\left(\frac{I_{1}}{3}\right)^{-\frac{1}{2}} - 48 \right]$$

$$+ \frac{\pi r^{2}}{a^{2}} \frac{\mu_{0}}{2} \left[\lambda_{1}^{2} + \lambda_{2}^{2} + \lambda_{3}^{2} + 2\left(\lambda_{1}^{-1} + \lambda_{2}^{-1} + \lambda_{3}^{-1}\right) - 24 \right].$$
(C-4)

• With Ogden model:

$$W(\lambda_{1}, \lambda_{2}, \lambda_{3}) = \frac{\pi r^{2}}{\sqrt{2}a^{2}} \sum_{p=1}^{N} \frac{2\mu_{p}}{\alpha_{p}^{2}} \left[4\left(\frac{1}{2}\lambda_{1}^{2} + \frac{1}{2}\lambda_{2}^{2}\right)^{\frac{a_{p}}{2}} + 4\left(\frac{1}{2}\lambda_{2}^{2} + \frac{1}{2}\lambda_{3}^{2}\right)^{\frac{a_{p}}{2}} + 4\left(\frac{1}{2}\lambda_{3}^{2} + \frac{1}{2}\lambda_{1}^{2}\right)^{\frac{a_{p}}{2}} + 4\left(\frac{1}{2}\lambda_{3}^{2} + \frac{1}{2}\lambda_{1}^{2}\right)^{\frac{a_{p}}{2}} + 4\left(\frac{1}{2}\lambda_{3}^{2} + \frac{1}{2}\lambda_{1}^{2}\right)^{\frac{a_{p}}{2}} + 4\left(\frac{1}{2}\lambda_{3}^{2} + \frac{1}{2}\lambda_{1}^{2}\right)^{\frac{a_{p}}{4}} + 8\left(\frac{1}{2}\lambda_{3}^{2} + \frac{1}{2}\lambda_{1}^{2}\right)^{\frac{a_{p}}{4}} - 36\right] + \frac{\sqrt{3}\pi r^{2}}{2a^{2}} \sum_{p=1}^{N} \frac{2\mu_{p}}{\alpha_{p}^{2}} \left[16\left(\frac{I_{1}}{3}\right)^{\frac{a_{p}}{2}} + 32\left(\frac{I_{1}}{3}\right)^{-\frac{a_{p}}{4}} - 48\right] + \frac{\pi r^{2}}{a^{2}} \sum_{p=1}^{N} \frac{2\mu_{p}}{\alpha_{p}^{2}} \left[\lambda_{1}^{a_{p}} + \lambda_{2}^{a_{p}} + \lambda_{3}^{a_{p}} + 2\left(\lambda_{1}^{\frac{a_{p}}{2}} + \lambda_{2}^{\frac{a_{p}}{2}} + \lambda_{3}^{\frac{a_{p}}{2}}\right) - 9\right]$$
(C-5)

• With Arruda-Boyce model:

$$W(\lambda_{1},\lambda_{2},\lambda_{3}) = \frac{\pi r^{2}}{\sqrt{2}a^{2}} u_{0} \left(\frac{1}{2} \left[+16(2\lambda_{1}^{2} + 2\lambda_{2}^{2})^{-1/2} + 16(2\lambda_{2}^{2} + 2\lambda_{3}^{2})^{-1/2} + 16(2\lambda_{3}^{2} + 2\lambda_{1}^{2})^{-1/2} \right] + 16(2\lambda_{3}^{2} + 2\lambda_{1}^{2})^{-1/2} + 16(2\lambda_{3}^{2}$$

C.3. Octahedral Lattice

· With neo-Hookean model:

$$W(\lambda_1, \lambda_2, \lambda_3) = \frac{\sqrt{3}\pi r^2}{2a^2} \frac{\mu_0}{2} \left[8\left(\frac{I_1}{3}\right) + 16\left(\frac{I_1}{3}\right)^{-\frac{1}{2}} - 24 \right]. \tag{C-7}$$

• With Ogden model:

$$W(\lambda_1, \lambda_2, \lambda_3) = \frac{\sqrt{3}\pi r^2}{2a^2} \sum_{p=1}^{N} \frac{2\mu_p}{a_p^2} \left[8\left(\frac{I_1}{3}\right)^{\frac{a_p}{2}} + 16\left(\frac{I_1}{3}\right)^{-\frac{a_p}{4}} - 24 \right].$$
 (C-8)

References

Ablowitz, M.J., Fokas, A.S., Fokas, A.S., 2003. Complex variables: Introduction and Applications. Cambridge University Press.

Ajdari, A., Jahromi, B.H., Papadopoulos, J., Nayeb-Hashemi, H., Vaziri, A., 2012. Hierarchical honeycombs with tailorable properties. Int. J. Solids Struct. 49, 1413–1419.

An, N., Domel, A.G., Zhou, J., Rafsanjani, A., Bertoldi, K., 2020. Programmable hierarchical kirigami. Adv. Funct. Mater. 30, 1906711.

Arruda, E.M., Boyce, M.C., 1993. A three-dimensional constitutive model for the large stretch behavior of rubber elastic materials. J. Mech. Phys. Solids 41, 389–412.

Berger, J., Wadley, H., McMeeking, R., 2017. Mechanical metamaterials at the theoretical limit of isotropic elastic stiffness. Nature 543, 533-537.

Chen, Y., Jia, Z., Wang, L., 2016. Hierarchical honeycomb lattice metamaterials with improved thermal resistance and mechanical properties. Compos. Struct. 152, 395–402

Clausen, A., Wang, F., Jensen, J.S., Sigmund, O., Lewis, J.A., 2015. Topology optimized architectures with programmable poisson's ratio over large deformations.

Adv. Mater. 27, 5523–5527

Deshpande, V.S., Fleck, N.A., Ashby, M.F., 2001. Effective properties of the octet-truss lattice material. J. Mech. Phys. Solids 49, 1747-1769.

Elsayed, M.S., Pasini, D., 2010. Analysis of the elastostatic specific stiffness of 2d stretching-dominated lattice materials. Mech. Mater. 42, 709-725.

Evans, K.E., Alderson, A., 2000. Auxetic materials: functional materials and structures from lateral thinking! Adv. Mater. 12, 617-628.

Fleck, N., Deshpande, V., Ashby, M., 2010. Micro-architectured materials: past, present and future. Proc. R. Soc. Lond. A: Math. Phys. Eng. Sci. 466, 2495–2516. Gibson, L.J., Ashby, M.F., 1999. Cellular solids: Structure and Properties. Cambridge university press.

Haghpanah, B., Oftadeh, R., Papadopoulos, J., Vaziri, A., 2013. Self-similar hierarchical honeycombs. Proc. R. Soc. Lond. A: Math. Phys. Eng. Sci. 469, 20130022. Jamshidian, M., Boddeti, N., Rosen, D., Weeger, O., 2020. Multiscale modelling of soft lattice metamaterials: micromechanical nonlinear buckling analysis, experimental verification, and macroscale constitutive behaviour. Int. J. Mech. Sci. 188, 105956.

Jens, B., R, M.L., A, S.T., Ruth, S., Xiaoyu, Z., Lorenzo, V., 2017. Nanolattices: an emerging class of mechanical metamaterials. Adv. Mater. 29, 1701850.

Ji, Z., Zhang, X., Yan, C., Jia, X., Xia, Y., Wang, X., Zhou, F., 2019. 3d printing of photocuring elastomers with excellent mechanical strength and resilience. Macromol. Rapid Commun. 40, 1800873.

Jiang, Y., Wang, Q., 2016. Highly-stretchable 3d-architected mechanical metamaterials. Sci. Rep. 6, 34147.

Jivkov, A.P., Yates, J.R., 2012. Elastic behaviour of a regular lattice for meso-scale modelling of solids. Int. J. Solids Struct. 49, 3089-3099.

Kadic, M., Milton, G.W., van Hecke, M., Wegener, M., 2019. 3d metamaterials. Nat. Rev. Phys. 1, 198-210.

Kolpakov, A., 1985. Determination of the average characteristics of elastic frameworks. J. Appl. Math. Mech. 49, 739-745.

Lakes, R., 1987. Foam structures with a negative poisson's ratio. Science 235, 1038–1041.

Lakes, R., 1996. Cellular solid structures with unbounded thermal expansion. J. Mater. Sci. Lett. 15, 475-477.

Lanczos, C., 2012. The Variational Principles of Mechanics. Courier Corporation.

Laubie, H., Monfared, S., Radjaï, F., Pellenq, R., Ulm, .F.,-J., 2017a. Effective potentials and elastic properties in the lattice-element method: isotropy and transverse isotropy. J. Nanomech. Micromech. 7, 04017007.

Laubie, H., Radjai, F., Pellenq, R., Ulm, F.,-J., 2017b. A potential-of-mean-force approach for fracture mechanics of heterogeneous materials using the lattice element method. J. Mech. Phys. Solids 105, 116–130.

Li, T., Jiang, Y., Yu, K., Wang, Q., 2017. Stretchable 3d lattice conductors. Soft Matter 13, 7731-7739.

Lin, Z., Novelino, L.S., Wei, H., Alderete, N.A., Paulino, G.H., Espinosa, H.D., Krishnaswamy, S., 2020. Folding at the microscale: enabling multifunctional 3d origamiarchitected metamaterials. Small 16, 2002229.

Liska, R., Schwager, F., Maier, C., Cano-Vives, R., Stampfl, J., 2005. Water-soluble photopolymers for rapid prototyping of cellular materials. J. Appl. Polym. Sci. 97, 2286–2298.

Meza, L.R., Zelhofer, A.J., Clarke, N., Mateos, A.J., Kochmann, D.M., Greer, J.R., 2015. Resilient 3d hierarchical architected metamaterials. Proc. Natl. Acad. Sci. 112, 11502–11507.

Montemayor, L., Chernow, V., Greer, J.R., 2015. Materials by design: using architecture in material design to reach new property spaces. MRS Bull. 40, 1122–1129. Mousanezhad, D., Babaee, S., Ebrahimi, H., Ghosh, R., Hamouda, A.S., Bertoldi, K., Vaziri, A., 2015. Hierarchical honeycomb auxetic metamaterials. Sci. Rep. 5, 1–8. Oftadeh, R., Haghpanah, B., Papadopoulos, J., Hamouda, A., Nayeb-Hashemi, H., Vaziri, A., 2014a. Mechanics of anisotropic hierarchical honeycombs. Int. J. Mech. Sci. 81, 126–136.

Oftadeh, R., Haghpanah, B., Vella, D., Boudaoud, A., Vaziri, A., 2014b. Optimal fractal-like hierarchical honeycombs. Phys. Rev. Lett. 113, 104301.

Ogden, R.W., 1972. Large deformation isotropic elasticity—on the correlation of theory and experiment for incompressible rubberlike solids. Proc. R. Soc. Lond. A. Math. Phys. Sci. 326, 565–584.

Pugh, C.C., Pugh, C., 2002. Real Mathematical Analysis. Springer.

Rivlin, R., 1948. Large elastic deformations of isotropic materials. I. Fundamental concepts. Philos. Trans. R. Soc. Lond. Series A Math. Phys. Sci. 240, 459–490. Roper, C.S., Schubert, R.C., Maloney, K.J., Page, D., Ro, C.J., Yang, S.S., Jacobsen, A.J., 2015. Scalable 3d bicontinuous fluid networks: polymer heat exchangers toward artificial organs. Adv. Mater. 27, 2479–2484.

Rubinstein, M., Colby, R.H., 2003. Polymer Physics. Oxford university press, New York.

Rubinstein, M., Panyukov, S., 2002. Elasticity of polymer networks. Macromolecules 35, 6670-6686.

Rudin, W., 1964. Principles of Mathematical Analysis. McGraw-hill, New York.

Sanami, M., Ravirala, N., Alderson, K., Alderson, A., 2014. Auxetic materials for sports applications. Procedia Eng 72, 453-458.

Schaedler, T.A., Carter, W.B., 2016, Architected cellular materials, Annu, Rev. Mater. Res. 46, 187–210.

Seo, S.I., Jang, C.D., 1996. Development of a rigid-ended beam element for analysis of bracketed frame structures. Mar. struct. 9, 971-990.

Surjadi, J.U., Gao, L., Du, H., Li, X., Xiong, X., Fang, N.X., Lu, Y., 2019. Mechanical metamaterials and their engineering applications. Adv. Eng. Mater. 21, 1800864. Tancogne-Dejean, T., Diamantopoulou, M., Gorji, M.B., Bonatti, C., Mohr, D., 2018. 3d plate-lattices: an emerging class of low-density metamaterial exhibiting optimal isotropic stiffness. Adv. Mater. 30, 1803334.

Timoshenko, S., 1983. History of Strength of materials: With a brief Account of the History of Theory of Elasticity and Theory of Structures. Courier Corporation. Treloar, L., 1943. The elasticity of a network of long-chain molecules. I. Trans. Faraday Soc. 39, 36–41.

Treloar, L.R.G., 1975. The Physics of Rubber Elasticity. Oxford University Press, Oxford.

Wadley, H.N., 2006. Multifunctional periodic cellular metals. Philos. Trans. R. Soc. Lond. Series A Math. Phys. Eng. Sci. 364, 31–68.

Wang, F., Sigmund, O., Jensen, J.S., 2014. Design of materials with prescribed nonlinear properties. J. Mech. Phys. Solids 69, 156-174.

Wang, Q., Jackson, J.A., Ge, Q., Hopkins, J.B., Spadaccini, C.M., Fang, N.X., 2016. Lightweight mechanical metamaterials with tunable negative thermal expansion. Phys. Rev. Lett. 117, 175901.

Wang, Y., Mora, P., 2008. Macroscopic elastic properties of regular lattices. J. Mech. Phys. Solids 56, 3459–3474.

Weeger, O., Boddeti, N., Yeung, S.-K., Kaijima, S., Dunn, M.L., 2019. Digital design and nonlinear simulation for additive manufacturing of soft lattice structures. Additive Manuf. 25, 39–49.

Wu, P., Van Der Giessen, E., 1993. On improved network models for rubber elasticity and their applications to orientation hardening in glassy polymers. J. Mech. Phys. Solids 41, 427–456.

Xu, C., Gallant, B.M., Wunderlich, P.U., Lohmann, T., Greer, J.R., 2015. Three-dimensional au microlattices as positive electrodes for li–o2 batteries. ACS Nano 9, 5876–5883.

Ye, H., Li, Y., Zhang, T., 2020. Magttice: a lattice model for hard-magnetic soft materials. Soft Matter.

Yu, K., Du, H., Xin, A., Lee, K.H., Feng, Z., Masri, S.F., Chen, Y., Huang, G., Wang, Q., 2020. Healable, memorizable, and transformable lattice structures made of stiff polymers. NPG Asia Mater. 12, 1–16.

Yu, K., Fang, N.X., Huang, G., Wang, Q., 2018. Magnetoactive acoustic metamaterials. Adv. Mater. 30, 1706348.

Zhang, M., Morrison, C.N., Jivkov, A.P., 2014. Meso-scale site-bond model for elasticity: theory and calibration. Mater. Res. Innov. 18. S2-982-S982-986.

Zheng, X., Smith, W., Jackson, J., Moran, B., Cui, H., Chen, D., Ye, J., Fang, N., Rodriguez, N., Weisgraber, T., 2016. Multiscale metallic metamaterials. Nat. Mater. 15, 1100–1106.